Article

Structural mechanisms for regulation of GSDMB pore-forming activity

https://doi.org/10.1038/s41586-023-05872-5

Received: 17 October 2022

Accepted: 21 February 2023

Published online: 29 March 2023

Check for updates

Xiu Zhong[1,2,10], Huan Zeng[2,3,4,10], Zhiwei Zhou[2,5,10], Ya Su[2,6], Hang Cheng[7], Yanjie Hou[3], Yang She[2], Na Feng[3], Jia Wang[2,3,4], Feng Shao[1,2,3,5,6,8,9] ✉ & Jingjin Ding[2,3,4] ✉

Cytotoxic lymphocyte-derived granzyme A (GZMA) cleaves GSDMB, a gasdermin-family pore-forming protein[1,2], to trigger target cell pyroptosis[3]. GSDMB and the charter gasdermin family member GSDMD[4,5] have been inconsistently reported to be degraded by the *Shigella flexneri* ubiquitin-ligase virulence factor IpaH7.8 (refs. [6,7]). Whether and how IpaH7.8 targets both gasdermins is undefined, and the pyroptosis function of GSDMB has even been questioned recently[6,8]. Here we report the crystal structure of the IpaH7.8–GSDMB complex, which shows how IpaH7.8 recognizes the GSDMB pore-forming domain. We clarify that IpaH7.8 targets human (but not mouse) GSDMD through a similar mechanism. The structure of full-length GSDMB suggests stronger autoinhibition than in other gasdermins[9,10]. GSDMB has multiple splicing isoforms that are equally targeted by IpaH7.8 but exhibit contrasting pyroptotic activities. Presence of exon 6 in the isoforms dictates the pore-forming, pyroptotic activity in GSDMB. We determine the cryo-electron microscopy structure of the 27-fold-symmetric GSDMB pore and depict conformational changes that drive pore formation. The structure uncovers an essential role for exon-6-derived elements in pore assembly, explaining pyroptosis deficiency in the non-canonical splicing isoform used in recent studies[6,8]. Different cancer cell lines have markedly different isoform compositions, correlating with the onset and extent of pyroptosis following GZMA stimulation. Our study illustrates fine regulation of GSDMB pore-forming activity by pathogenic bacteria and mRNA splicing and defines the underlying structural mechanisms.

Pyroptosis is crucial for immune defence against infections and endogenous dangers[11,12]. Pyroptosis is executed by the gasdermin family, whose members share an N-terminal pore-forming domain and a C-terminal autoinhibitory domain[1,2]. The charter family member gasdermin D (GSDMD)[4,5] carries out caspase-1 and caspase-11/caspase-4/caspase-5-mediated pyroptosis in canonical[13] and non-canonical[14,15] inflammasomes, respectively. The caspases cleave the interdomain linker in GSDMD; the unleashed GSDMD-N domain then perforates the plasma membrane to cause cell lysis[9,16]. *GSDMB* is absent in rodents and its polymorphism is associated with increased risks of asthma[17,18]. GSDMB is activated by granzyme A (GZMA) from natural killer cells and cytotoxic T lymphocytes through cleavage at K244 in the interdomain linker[3]. Pyroptotic killing of cancer cells by cytotoxic T lymphocytes stimulates potent anti-tumour immunity[3,19].

A recent study reported that *Shigella flexneri*, causative for shigellosis, uses a type III secretion system effector, IpaH7.8, to specifically ubiquitinate GSDMB for proteasomal degradation[6]. Another group also investigated IpaH7.8 inhibition of pyroptosis-mediated defences, but identified human (not mouse) GSDMD as its substrate[7]. The findings, although inconsistent, in both cases suggest a reason why *S. flexneri* causes bacillary dysentery in humans but not mice. Notably, the former study showed that GSDMB, following cleavage by natural-killer-cell-derived GZMA, did not cause pyroptosis but killed intracellular bacteria[6]. Another study on GSDMB in inflammatory bowel disease also claimed that it had a pyroptosis-null function in regulating intestinal epithelial maintenance and repair[8], again calling into question whether GSDMB is a pore-forming, pyroptotic protein.

Crystal structure of the IpaH7.8–GSDMB complex

We first observed that expression of IpaH7.8, but not its ubiquitin-ligase activity-deficient C357S mutant (IpaH7.8^{C357S}), efficiently degraded both GSDMB and GSDMD in 293T cells (Extended Data Fig. 1a). IpaH7.8^{C357S} specifically co-immunoprecipitated GSDMB among five human gasdermins (Extended Data Fig. 1b). IpaH family members share a diverse leucine-rich repeat (LRR) domain and a nearly identical C-terminal

[1]Peking University–Tsinghua University–National Institute of Biological Sciences Joint Graduate Program, School of Life Sciences, Tsinghua University, Beijing, PR China. [2]National Institute of Biological Sciences, Beijing, PR China. [3]National Laboratory of Biomacromolecules, CAS Center for Excellence in Biomacromolecules, Institute of Biophysics, Chinese Academy of Sciences, Beijing, PR China. [4]University of Chinese Academy of Sciences, Beijing, PR China. [5]Research Unit of Pyroptosis and Immunity, Chinese Academy of Medical Sciences and National Institute of Biological Sciences, Beijing, PR China. [6]Tsinghua Institute of Multidisciplinary Biomedical Research, Tsinghua University, Beijing, PR China. [7]Shuimu BioSciences, Beijing, PR China. [8]Changping Laboratory, Beijing, PR China. [9]New Cornerstone Science Laboratory, Shenzhen, PR China. [10]These authors contributed equally: Xiu Zhong, Huan Zeng, Zhiwei Zhou. ✉e-mail: shaofeng@nibs.ac.cn; jding@ibp.ac.cn

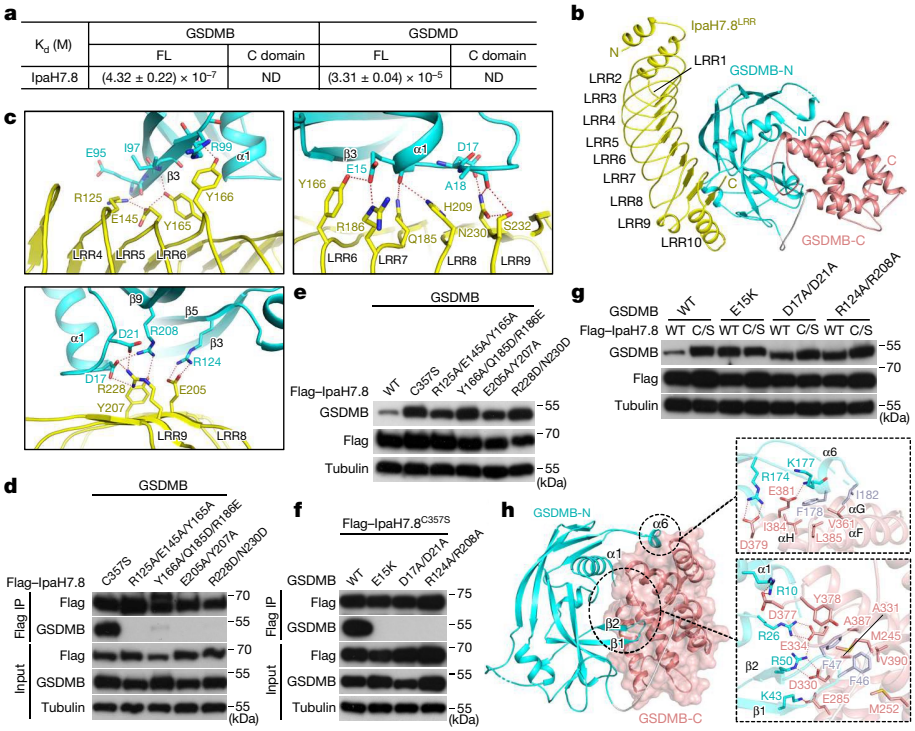

Fig. 1 | Structural basis for IpaH7.8 recognition of GSDMB and features of GSDMB autoinhibition. a, SPR measurements of the binding between IpaH7.8 and full-length (FL) or the C domain of GSDMB or GSDMD. K_d is shown as the mean ± s.d. from three determinations. ND, not detectable. **b**, Crystal structure of the IpaH7.8^{LRR}–GSDMB complex. The LRRs of IpaH7.8 are numbered. **c**, Interactions between IpaH7.8^{LRR} and GSDMB. The interaction residues are labelled and shown as sticks. Dotted lines represent hydrogen bonds. **d**–**g**, Co-immunoprecipitation (IP) (**d**,**f**) and GSDMB degradation (**e**,**g**) assays of the IpaH7.8–GSDMB binding interface. Flag–IpaH7.8 (WT, C357S or a binding site mutant) was co-expressed with GSDMB (WT or a binding site mutant) in 293T cells. **d**,**f**, Anti-Flag immunoprecipitation followed by immunoblotting. **e**,**g**, Immunoblotting of total lysates. **h**, Structural analyses of GSDMB autoinhibition. The GSDMB-N domain is shown as a cartoon, and structural elements binding the GSDMB-C domain (cartoon overlaid with a transparent surface) are labelled. The major and minor interfaces are highlighted by large and small dashed ellipses, respectively, with close-up views on the right. The interface residues are labelled and shown as sticks. Dotted lines represent hydrogen bonds. Data in **d**–**g** are representative of three independent experiments. See Supplementary Fig. 1 for gel source data.

ubiquitin-ligase domain[20]. The IpaH7.8 LRR domain (IpaH7.8^{LRR}) showed similar co-immunoprecipitation with GSDMB as full-length IpaH7.8 (Extended Data Fig. 1c). Purified full-length IpaH7.8 or IpaH7.8^{LRR} formed a 1:1 complex with GSDMB in gel-filtration chromatography (Extended Data Fig. 1d). Surface plasmon resonance (SPR) determined a binding constant (K_d) of about 432 nM (Fig. 1a and Extended Data Fig. 1e). IpaH7.8 did not bind to the GSDMB-C domain (Fig. 1a and Extended Data Fig. 1f), indicating recognition of the pore-forming domain.

We crystallized the IpaH7.8^{LRR}–GSDMB complex and solved the 2.7 Å structure (Fig. 1b and Extended Data Table 1). IpaH7.8^{LRR} adopts a solenoid-like shape; each of the ten LRRs (LRR1–LRR10) contributes one strand to form a parallel β-sheet, which makes up the solenoid concave. The N-terminal tandem, paired helices cover one end of the solenoid, while the other end is masked by a helix between LRR9 and LRR10 (Fig. 1b). IpaH7.8^{LRR} does not contact the GSDMB-C domain, and its solenoid concave perpendicularly covers the convex of the GSDMB-N domain (Fig. 1b). The interface is formed by LRR4–LRR9, which firmly interact with β3 and its nearby structure in the GSDMB-N domain. Specifically, R125, E145 and Y165–Y166 from the loop regions of LRR4, LRR5 and LRR6, respectively, form a hydrogen-bond network with the backbones of E95, I97 and R99 in β3 of GSDMB (Fig. 1c). Q185–R186, H209 and N230–S232 from the loops of LRR7, LRR8 and LRR9, respectively, form another series of hydrogen-bond contacts with E15, D17 and the backbone of A18 of GSDMB (Fig. 1c). The side chains of E205, Y207 and R228 from LRR8–LRR9 interact with R124, R208 and the nearby D17/D21 in the GSDMB-N domain (Fig. 1c).

Mutations mapping to the interface residues in IpaH7.8, such as the R125A/E145A/Y165A and Y166A/Q185D/R186E triple substitutions as well as the E205A/Y207A and R228D/N230D double substitutions, disrupted IpaH7.8–GSDMB binding in both 293T cells (Fig. 1d) and gel-filtration co-elution assays (Extended Data Fig. 1g). These mutants failed to elicit degradation of cellular GSDMB (Fig. 1e). Reciprocally, mutations mapping to IpaH7.8-interacting residues in GSDMB (E15K, D17A/D21A and R124A/R208A) also disrupted the IpaH7.8–GSDMB interaction (Fig. 1f and Extended Data Fig. 1h), resulting in resistance to degradation by IpaH7.8 (Fig. 1g). These data validate the structural basis for IpaH7.8 targeting of GSDMB.

Mechanisms of GSDMB autoinhibition

Among human gasdermins, the autoinhibited structure has only been solved for GSDMD[10], with extensive internal deletions used for crystallization. The autoinhibition mechanism, incompletely revealed in that structure, has some differences to that of mouse GSDMA3 (refs. [9,10]). Our IpaH7.8^{LRR}–GSDMB complex represents an intact, full-length GSDMB structure that would otherwise be extremely difficult to obtain. Like GSDMA3 and GSDMD[9,10,21], GSDMB adopts a two-domain architecture including a globular GSDMB-C domain of eight tandem helices (αA–αH) (Fig. 1h and Extended Data Fig. 2a). Of note, the linker between αG and αH is much shorter than that in other mammalian gasdermins, rendering GSDMB-C the smallest gasdermin C-domain (Extended Data Fig. 2a). The GSDMB-N domain features an extended twisted β-sheet of ten antiparallel strands (β1–β10) that, unlike in GSDMD, are all structurally ordered (Extended Data Fig. 2b). α1 and its following loop, together with the nearby β1/β2 hairpin, constitute a major interface with the

GSDMB-C domain (Fig. 1h). Surrounding the β-sheet are five helices (α2–α6) (Extended Data Fig. 2b); α6 protrudes away from the sheet to form a minor autoinhibition interface (Fig. 1h).

At the major interface, F46 and F47 are inserted into a hydrophobic pocket formed by M245, M252, A331, Y378, A387 and V390 of the GSDMB-C domain (Fig. 1h). Flanking the pocket are hydrogen bonds between R10, R26, K43 and R50 (GSDMB-N domain) and D377, E334, E285 and D330 (GSDMB-C domain), respectively. At the minor interface, F178 and I182 of α6 lie in a shallow non-polar pit formed by αF–αH of the GSDMB-C domain; R174 and the backbone of K177 form hydrogen bonds with D379 and E381 of αH in the GSDMB-C domain, respectively (Fig. 1h). Interactions at the two interfaces, particularly hydrophilic ones, are markedly more extensive than in GSDMD and GSDMA3 (refs. [9,10]), predicting stronger autoinhibition. Supporting this prediction, single-residue substitutions in the hydrophobic pocket, which are sufficient to activate GSDMD or GSDMA3 (refs. [9,10]), did not cause constitutive activation of GSDMB, and only combined mutations disrupting both hydrophobic and hydrogen-bond interactions at the major interface activated GSDMB to induce pyroptosis (Extended Data Fig. 2c). Compared with GSDMD, purified GSDMB exhibited slower kinetics in lysing liposomes following interdomain cleavage (Extended Data Fig. 2d). Moreover, overexpression of full-length GSDMB, unlike GSDMD, did not induce any spontaneous pyroptosis in 293T cells (Extended Data Fig. 2e). These data confirm the structural distinction of GSDMB and indicate that its pore-forming activity is more tightly controlled than that of other gasdermins.

A conserved mechanism to recognize GSDMD

IpaH7.8 could also efficiently target human GSDMD by recognizing its pore-forming domain (Fig. 1a and Extended Data Fig. 1a). Following structural superimposition, the pore-forming domains of GSDMD and GSDMB were roughly overlaid (Extended Data Fig. 3a). β3, α1 and the following turn that mediate GSDMB binding to IpaH7.8^{LRR} overlapped well with their counterparts in GSDMD (Extended Data Fig. 3a). Although the β3-corresponding region in GSDMD is not a strand (Extended Data Fig. 2b), its extended, fixed conformation could probably support most of the backbone interactions with IpaH7.8^{LRR}. Despite conformational deviations between the two gasdermins (Extended Data Fig. 3a), the sequences of α1 and the turn are conserved, particularly the acidic residues (E15, D17 and D21 in GSDMB) that critically bind IpaH7.8^{LRR} (Extended Data Fig. 3c,d). Conformation adjustment of this region in GSDMD could result in similar binding to IpaH7.8. Indeed, all mutations in IpaH7.8 disrupting its interaction with GSDMB also blocked degradation of GSDMD and reversed pyroptosis inhibition (Extended Data Fig. 3b,e). Thus, IpaH7.8 probably targets GSDMD through a mechanism akin to that identified in the structure for the IpaH7.8–GSDMB complex. Notably, human GSDMD was only weakly co-immunoprecipitated by IpaH7.8 and no IpaH7.8–GSDMD complex was identified in gel-filtration chromatography (Extended Data Fig. 1b–d); the K_d was 76 times higher than that of GSDMB and IpaH7.8 (Fig. 1a and Extended Data Fig. 1e). The compromised binding is probably due to the structural differences between the GSDMD-N domain and the GSDMB-N domain. For instance, R124 of GSDMB, which forms strong binate hydrogen bonds with E205 of IpaH7.8^{LRR}, is a serine residue in GSDMD (Extended Data Fig. 3c).

Compared with human GSDMD, mouse GSDMD bears an insertion (G18) and two substitutions (D17S and G20R) at the C terminus of α1 (Extended Data Fig. 3d). These differences are predicted to disrupt binding to IpaH7.8, as confirmed by the SPR data (Extended Data Fig. 1e). Accordingly, mouse GSDMD resisted degradation by IpaH7.8 in 293T cells, and substituting L16–E21 in human GSDMD with the mouse sequence (V16–D22) also rendered the protein resistant to degradation (Extended Data Fig. 3f). Other gasdermins all have unfavourable substitutions in crucial IpaH7.8-binding residues (Extended Data Fig. 3c), in line with the lack of co-immunoprecipitation (Extended Data Fig. 1b,c). These data explain why only GSDMB and human GSDMD are degraded by IpaH7.8.

Analyses of GSDMB isoforms

GSDMD has one transcript, whereas ten *GSDMB* variants are recorded in the NCBI database, producing five isoforms (GSDMB^{iso1} to GSDMB^{iso5}) (Extended Data Fig. 4a). In GSDMB^{iso1} to GSDMB^{iso4}, the GSDMB-C domain and the core regions of the GSDMB-N domain are identical. The sequence differences, resulting from alternative splicing of exons 6 and 7, lie in the C terminus of the GSDMB-N domain and the interdomain linker (Fig. 2a). GSDMB^{iso3} contains all sequences derived from the two exons, whereas GSDMB^{iso2} lacks both; GSDMB^{iso4} and GSDMB^{iso1} have only exon-6- and exon-7-derived sequences, respectively. Structural elements mediating recognition by IpaH7.8, identified in the structure for the IpaH7.8^{LRR}–GSDMB^{iso4} complex, are present in all four isoforms. In line with this, IpaH7.8 showed comparable co-immunoprecipitation interaction and complex formation with the four isoforms and readily induced their degradation in 293T cells (Fig. 2b,c and Extended Data Fig. 4b). GSDMB^{iso5} lacks not only exon-6- and exon-7-derived sequences but also 28 residues of the GSDMB-N domain and 53 residues of the GSDMB-C domain (Extended Data Fig. 4a) and is probably misfolded.

The GZMA-cleavage site is present in GSDMB^{iso1} to GSDMB^{iso4}, which all can be targeted by GZMA[3]. We expected that IpaH7.8 would counteract GZMA-induced pyroptosis regardless of the GSDMB isoform. Supporting this prediction, no pyroptosis was observed in GZMA-stimulated 293T cells expressing wild-type (WT) IpaH7.8 and any of the GSDMB isoforms (Fig. 2c). When IpaH7.8^{C357S} or red fluorescent protein (RFP) was coexpressed with GSDMB, GZMA still did not induce pyroptosis in cells expressing GSDMB^{iso1} or GSDMB^{iso2} (Fig. 2d and Extended Data Fig. 4c). Echoing this finding, when GSDMB containing a PreScission protease (PPase) site (after the GZMA site) was expressed in 293T cells, delivery of PPase triggered pyroptosis in only GSDMB^{iso3}- or GSDMB^{iso4}-expressing cells, although the four isoforms were equally cleaved by PPase (Fig. 2e and Extended Data Fig. 4d).

Isoform-dependent pore-forming activity

The above analyses indicate that GSDMB isoforms may have different pyroptotic activity. Supporting this idea, expression of the GSDMB^{iso1}-N and GSDMB^{iso2}-N domains, in contrast to the GSDMB^{iso3}-N or GSDMB^{iso4}-N domain, did not elicit pyroptosis in 293T cells (Fig. 2f and Extended Data Fig. 5a). Additionally, unlike the GSDMB^{iso3}-N and GSDMB^{iso4}-N domains, expression of the GSDMB^{iso1}-N or GSDMB^{iso2}-N domain in *Escherichia coli* did not inhibit bacterial growth (Extended Data Fig. 5b,c). Like other active gasdermins[9], purified GSDMB^{iso3} and GSDMB^{iso4} proteins, after interdomain cleavage, could not kill *S. flexneri* owing to the lack of lipid targets in the bacterial outer membrane (Extended Data Fig. 5d–f). In liposome leakage assays, lysis activities were not recorded for GSDMB^{iso1} or GSDMB^{iso2}, whereas GSDMB^{iso3} and GSDMB^{iso4} exhibited strong activities on liposomes containing PI(4,5)P_2 or cardiolipin (Extended Data Fig. 5g–i). Negative-stain electron microscopy (EM) directly confirmed the presence and absence of pore-forming activity in the GSDMB^{iso3}-N/GSDMB^{iso4}-N domains and GSDMB^{iso1}-N/GSDMB^{iso2}-N domains, respectively (Fig. 2g). These data establish isoform-dependent pore-forming activities in GSDMB, which underlie the contrasting functions of the isoforms in induction of pyroptosis.

Cryo-EM structure of the GSDMB pore

To understand the isoform-dependent pore-forming activity, we tried to solve the pore structure of GSDMB using single-particle cryo-EM (Extended Data Fig. 6a). Lauryl maltose neopentyl glycol (LMNG) was identified as the best detergent to solubilize GSDMB^{iso4} pores from cardiolipin liposomes supplemented with a small amount of phosphatidic acid. Following gel-filtration chromatography, purified pores were subjected to negative-stain EM and cryo-EM data collection (Extended Data Fig. 6a–c). Two-dimensional (2D) classification showed 26- to 30-fold

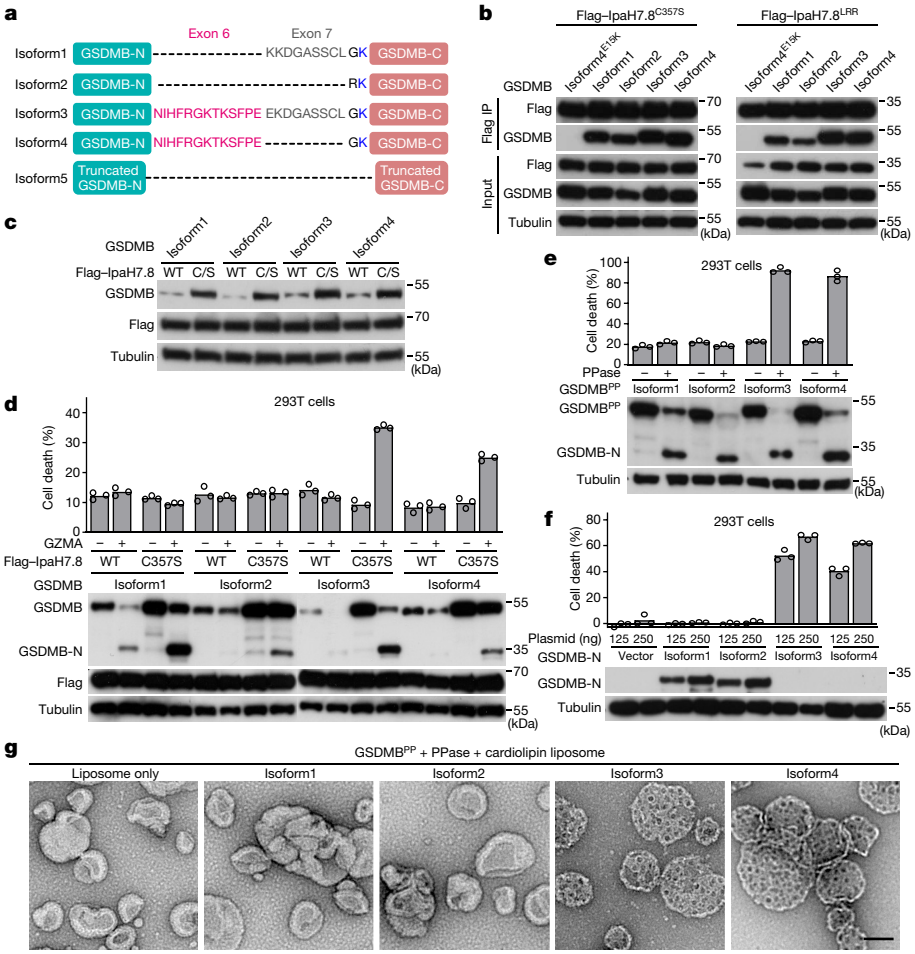

Fig. 2 | GSDMB isoforms are equally targeted by IpaH7.8 but exhibit different pore-forming activities. a, Diagram of the five *GSDMB* splicing isoforms found in the NCBI database. **b**, Co-immunoprecipitation of IpaH7.8^{C357S} or IpaH7.8^{LRR} with different GSDMB isoforms in 293T cells. Cell lysates were subjected to anti-Flag immunoprecipitation and immunoblotting. **c**, Flag–IpaH7.8 (WT or C357S) was coexpressed with a GSDMB isoform in 293T cells. Cell lysates were subjected to immunoblotting. **d**, Assays of GSDMB isoforms in IpaH7.8 blocking of GZMA-induced pyroptosis. Construct encoding Flag–IpaH7.8 (WT or C357S) was transfected into 293T cells stably expressing a GSDMB isoform; GZMA was electroporated into the cells. **e**,**f**, Assays of pyroptotic activity in GSDMB isoforms. **e**, PPase was electroporated into 293T cells stably expressing a GSDMB isoform bearing a PPase site (GSDMB^{PP}). **f**, Constructs encoding the N domains of the GSDMB isoforms were transfected into 293T cells. In **d**–**f**, lactate dehydrogenase (LDH) release-based cell death data are shown as the mean (bars) of three replicates (circles). In **d**,**e**, cell lysates were immunoblotted to probe GSDMB degradation and/or cleavage. **g**, Negative-stain EM assays of pore-forming activities in different GSDMB isoforms on cardiolipin liposomes. Scale bar, 100 nm. All data are representative of three independent experiments. See Supplementary Fig. 1 for gel source data.

symmetry in GSDMB pores, with the majority of pores containing 26, 27 (>50%) or 28 protomers (Extended Data Fig. 6d). Such variability in symmetry was also noted with GSDMB^{iso3} (Extended Data Fig. 6e), as well as with the GSDMD and GSDMA3 pores[22,23]. After iterative 2D averaging and three-dimensional (3D) reconstitution (Extended Data Fig. 6f), data for the 27-fold-symmetric pores yielded the best density map with the resolution reaching 3.2 Å (Extended Data Fig. 7a and Extended Data Table 2). The structure was solved using the GSDMB-N domain crystal structure as an initial model (Extended Data Fig. 7b,c). The pore has inner and outer diameters of about 160 Å and 270 Å, respectively, close to those of the 27-mer GSDMA3 pore[22] (Fig. 3a). Like the GSDMA3 and GSDMD pores, the GSDMB pore features a coronary ring and a transmembrane β-barrel ring, organized by the large globular subdomain and two side-by-side extended β-hairpins of the GSDMB-N domain, respectively (Fig. 3a). In the pore, the GSDMB-N domain refolds into a hand shape, with the globular subdomain forming the 'palm' and the β-hairpins corresponding to the 'fingers' (Fig. 3b). The angle between the palm and the fingers is reduced by about 9° and 38° relative to those in the GSDMA3-N and GSDMD-N pore protomers, respectively (Fig. 3c), rendering the globular subdomain in the GSDMB pore the most proximal to the membrane.

Structural comparison of the GSDMB-N domain in the autoinhibited state (from the IpaH7.8^{LRR}–GSDMB complex) with that in the pore showed conformational changes similar to those seen in GSDMA3 (ref. [22]) (Fig. 3d). Of note, the long frizzy loop linking α3 and β3 on the top face of the globular subdomain becomes ordered in the pore state; residues 82–89 form a strand that pushes β3 along its strand direction, being fused together into a new extended β3 (Fig. 3d). The linker containing the short β4 also refolds as a β-turn and a strand that merges with the original β5 to become an extended β4 (Fig. 3d). The new β3 and β4 form a large antiparallel β-hairpin. Additionally, the linker containing α6 turns into two antiparallel strands that are combined with the original β7 and β8 to form another large hairpin (β6/β7) (Fig. 3d). The β3/β4 and β6/β7 hairpins, arranged side by side, protrude from the globular subdomain for membrane insertion.

The turn of the β1/β2 hairpin at the bottom face of the globular subdomain becomes exposed in the pore state (Figs. 1h and 3c). In GSDMD, this β-turn bears two aromatic residues proposed as a membrane anchor with their side chains embedded into the phospholipid layer[23]. The corresponding residues in GSDMB (F46 and F47) probably have the same role (Fig. 3e,f). Adjacent to the anchor are two clusters of positively charged residues, forming basic surface sites that can interact with the polar

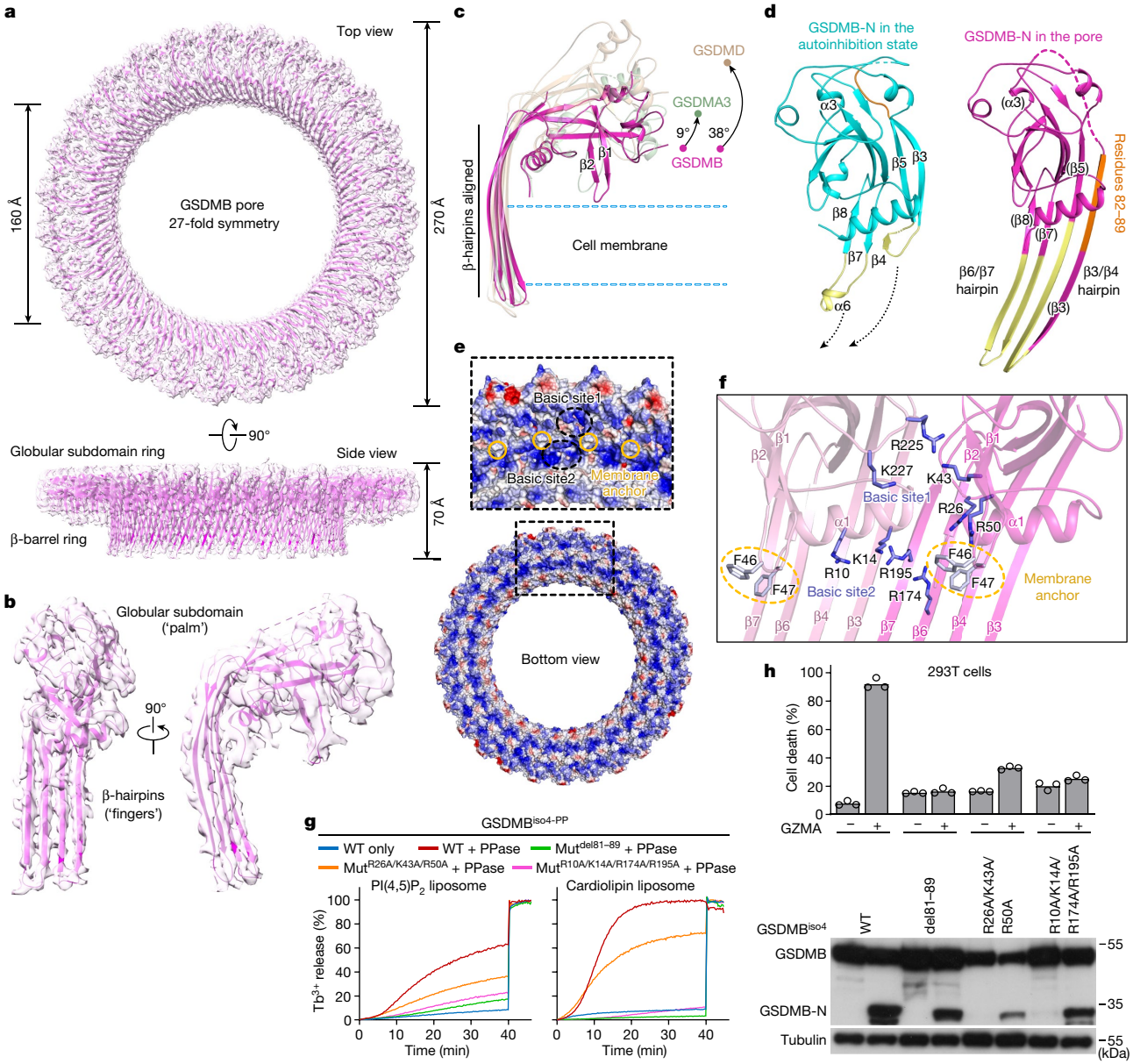

Fig. 3 | Cryo-EM structure of the GSDMB pore shows key conformational changes for pore formation. a, Ribbon scheme and dimensions of the 27-subunit GSDMB pore structure fitted into the cryo-EM density. **b**, Cartoon model of the GSDMB pore subunit fitted into the cryo-EM density. **c**, Structural comparison of the GSDMB pore subunit with the GSDMD (Protein Data Bank (PDB): 6VFE) and GSDMA3 (PDB: 6CB8) pores. Orientation deviation of the globular subdomain from the transmembrane β-hairpin is shown on the right. **d**, Comparison of the GSDMB-N domain in the autoinhibited structure and the pore structure. Conformationally changed structural elements are labelled and highlighted by colour. **e**, Electrostatic surface of the GSDMB pore. A close-up view on the right shows the hydrophobic membrane anchor and the two basic sites for acidic phospholipid binding, located at the bottom of the globular subdomain. **f**, Potential phospholipid-binding sites in the GSDMB pore subunit. Two neighbouring pore subunits are shown as cartoons. Residues forming the membrane anchor and the basic sites are shown as sticks. **g**,**h**, Functional analyses of conformational changes and phospholipid-binding sites of the GSDMB pore subunit. **g**, The indicated liposomes were treated with purified GSDMB^{PP} (WT or the indicated mutant) in the presence of PPase. Liposome leakage was assayed by measuring 2,6-pyridinedicarboxylic acid (DPA) chelating-induced fluorescence of released Tb^{3+}. **h**, 293T cells expressing GSDMB (WT or the indicated mutant) were electroporated with GZMA. LDH release-based cell death data are shown as the mean (bars) of three replicates (circles). The immunoblot shows the cleavage of GSDMB. Data in **g**,**h** are representative of three independent experiments. See Supplementary Fig. 1 for gel source data.

heads of the acidic phospholipids (Fig. 3e). Site 1 consists of R50/R26/K43 of one GSDMB-N protomer and R225/K227 from the C-terminal tail of a neighbouring protomer (Fig. 3f). Site 2, situated at the groove between the globular subdomain and the transmembrane hairpins, is formed by R174/R195 from the β6/β7 hairpin of one protomer and R10/K14 from α1 of the neighbouring protomer (Fig. 3f). The structural analyses were supported by mutagenesis analyses. Deletion of residues 81–89 in GSDMB that block formation of the β3/β4 hairpin abolished liposome leakage activity and GZMA-induced pyroptosis (Fig. 3g,h). Disruption of basic sites 1 and 2 by R26A/K43A/R50A triple and R10A/K14A/R195A/R174A quadruple substitution, respectively, had similar effects (Fig. 3g,h).

GSDMB oligomerization for pore assembly

Gasdermin pore assembly requires interactions between neighbouring protomers in both the globular subdomain and the transmembrane β-hairpins. In the GSDMB pore, β7 of each protomer flanks β3 of the neighbouring protomer in an antiparallel manner through extensive

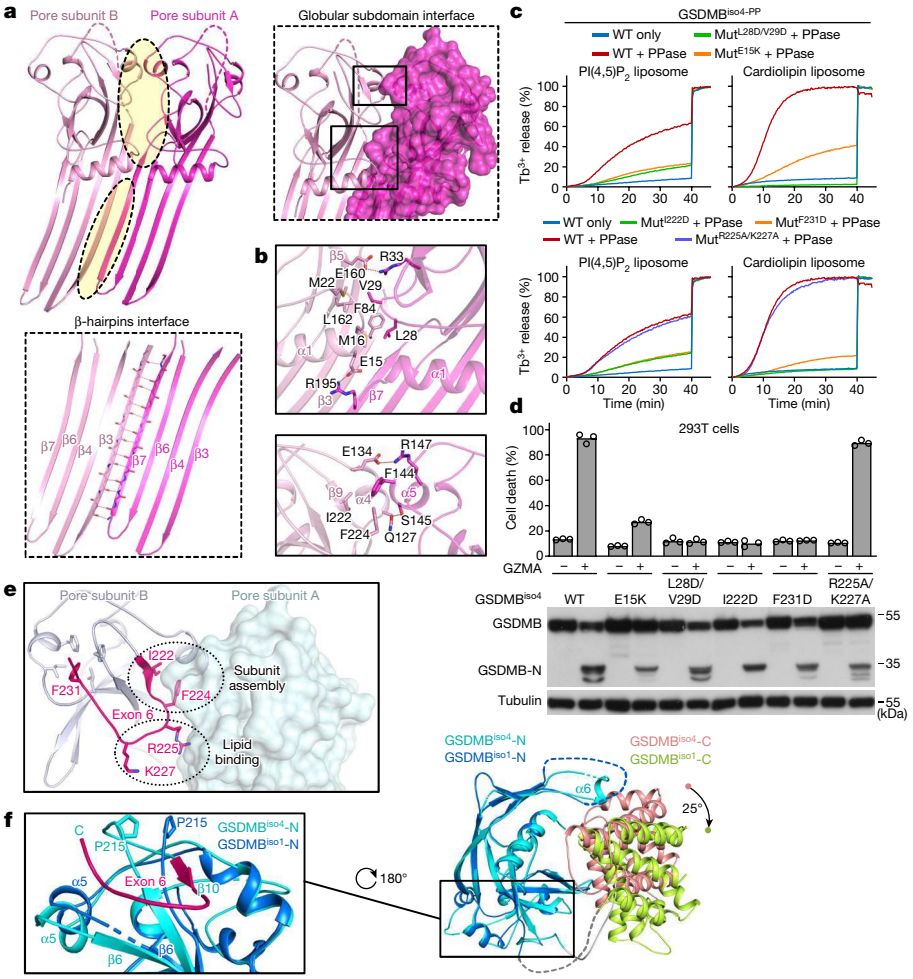

Fig. 4 | Structural basis for subunit assembly in the GSDMB pore and exon-6-dictated pore-forming activity. a, Structure of the inter-subunit interfaces in the GSDMB pore. Two neighbouring subunits are shown as cartoons. The interfaces between the two globular subdomains and the two transmembrane β-hairpins are highlighted, with close-up views on the right and the bottom, respectively. The globular subdomain interface has two binding sites (highlighted by boxes); the β-hairpin interface features extensive hydrogen bonds (dotted lines) formed by the backbones of β7 from one subunit and β3 from the neighbouring one. **b**, Interactions at the globular subdomain interface. Interaction residues from one GSDMB subunit are labelled. Dotted lines represent hydrogen bonds. **c**,**d**, Functional analyses of subunit assembly interactions in the GSDMB pore. **c**, The indicated liposomes were treated with purified GSDMB^{PP} (WT or the indicated mutant) in the presence of PPase. Liposome leakage was monitored by measuring DPA chelating-induced fluorescence of released Tb^{3+}. **d**, 293T cells expressing GSDMB (WT or the indicated mutant) were electroporated with GZMA. LDH release-based cell death data are shown as the mean (bars) of three replicates (circles). The immunoblot shows the cleavage of GSDMB. **e**, Structure of the exon-6-derived sequence in the GSDMB pore. Two neighbouring GSDMB subunits are shown as a cartoon and a transparent surface. The structure of the exon-6-derived sequence in one subunit is highlighted by colour. Exon 6 residues crucial for pore formation are labelled and shown as sticks. **f**, Cartoon structural comparison of GSDMB^{iso4} and GSDMB^{iso1}, aligned by their GSDMB-N domains. Orientation deviation of the GSDMB-C domain is shown on the right. The left close-up view shows structural differences around the exon-6-derived region between the two isoforms. Data in **c**,**d** are representative of three independent experiments. See Supplementary Fig. 1 for gel source data.

backbone hydrogen bonds, integrating the four-stranded β-hairpins from all protomers into a transmembrane β-barrel (Fig. 4a), resembling assembly of the GSDMA3 and GSDMD pores[22,23]. To form the coronary ring, two convex surface areas on each protomer are wedged into two concave pockets in the adjacent protomer (Fig. 4a). One convex surface features L28 and V29, which insert their side chains into a pocket formed by M16, M22, F84 and L162 of the neighbouring protomer, around which are two pairs of charge interactions, that is, R33 and R195 with E160 and E15, respectively (Fig. 4b). The other convex is mainly contributed by the outer face of α5; S145 and R147 form two separate hydrogen bonds with Q127 and E134 on α4 of the neighbouring protomer, and F144 interacts hydrophobically with I222/F224 from β9 of that protomer (Fig. 4b). Supporting the structural observations, aspartate substitution of L28 and V29 abolished the liposome leakage activity and pyroptosis-inducing function of GSDMB (Fig. 4c,d). The GSDMB E15K mutant also showed markedly attenuated pore-forming and pyroptotic activities, echoing the findings for GSDMA3 and GSDMD[22,23].

Structural basis of isoform differences

We have demonstrated that exon 6-encoded sequences, present in GSDMB^{iso3} and GSDMB^{iso4} but absent in GSDMB^{iso1} and GSDMB^{iso2}, dictate pore-forming activity. In the autoinhibited GSDMB^{iso4} structure, the 13 residues derived from exon 6 (N221–E233) form β10 and the ordered tail of the GSDMB-N domain that folds back to the top face of the globular subdomain (Extended Data Fig. 8a). This region adopts the same structure in the pore state (Extended Data Fig. 8a) but has multiple crucial roles in pore assembly (Fig. 4e). I222 and F224 from β9 (that is, β10 in the autoinhibited structure) participate in protomer oligomerization through hydrophobic interactions (Fig. 4b,e). F231 from the tail falls

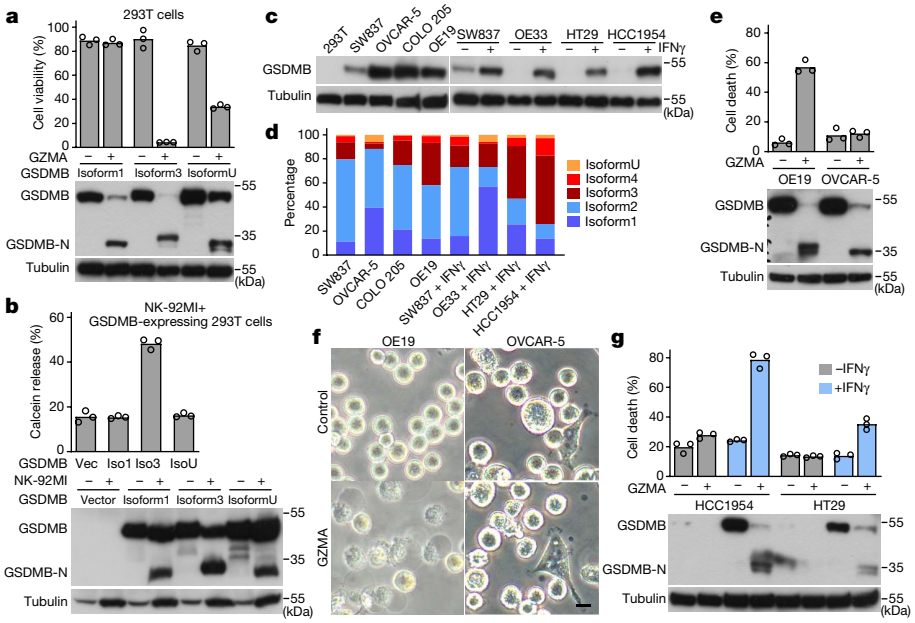

Fig. 5 | Implications of isoform-dependent pore-forming activities in GSDMB. a,**b**, Analyses of pyroptosis-inducing activity for the UniProt isoform (IsoU) of GSDMB. 293T cells stably expressing the indicated isoform were electroporated with GZMA (**a**) or subjected to killing by NK-92MI cells for 6 h (**b**). Cleavage of GSDMB was followed by immunoblotting. **a**, ATP-based cell viability data are shown as the mean (bars) of three replicates (circles). **b**, Pyroptosis was quantified by measuring calcein release from GSDMB-expressing cells, expressed as the mean (bars) of three replicates (circles). **c**, Immunoblotting of endogenous GSDMB expression in various cancer cell lines with or without IFNγ stimulation. **d**, Profiling GSDMB isoforms and their proportions in various cancer cell lines. **e**–**g**, Correlation between GSDMB isoform expression and GZMA-induced pyroptosis. GZMA was electroporated into the indicated cancer cell lines with or without IFNγ stimulation. **e**,**g**, LDH release-based cell death data are shown as the mean (bars) of three replicates (circles); immunoblots show the cleavage of GSDMB. **f**, Morphological analyses of cell pyroptosis. Scale bar, 25 μm. Data are representative of three (**a**–**c**,**e**–**g**) or two (**d**) independent experiments. See Supplementary Fig. 1 for gel source data.

into a hydrophobic pocket on the top face of the globular subdomain to stabilize the tail conformation (Fig. 4e). Alteration of either I222 or F231 abolished the pore-forming and pyroptotic activities of GSDMB (Fig. 4c,d), highlighting the importance of exon-6-derived structures for pore assembly. Alteration of R225 and K227 in the tail did not affect the activities of GSDMB (Fig. 4c,d), indicating that these residues may not have a key role in binding phospholipids in the membrane.

To understand the lack of pore-forming activity in GSDMB^{iso1} and GSDMB^{iso2}, we solved the 3.1 Å crystal structure of GSDMB^{iso1} (in complex with IpaH7.8^{LRR}) (Extended Data Table 1). GSDMB^{iso1} binds IpaH7.8 identically to GSDMB^{iso4} (Extended Data Fig. 8b), but the structures of the two isoforms have three prominent differences. First, the orientation of the GSDMB-C domain relative to the GSDMB-N domain is shifted by about 25° in GSDMB^{iso1} compared with GSDMB^{iso4} (Fig. 4f). This eliminates the minor interdomain interface and causes unfolding of α6. Second, owing to the absence of the exon-6-derived sequence, GSDMB^{iso1} does not have β10 and the following tail, both of which are important for pore assembly. Third, the structure of the C terminus of the GSDMB^{iso1}-N domain is notably different to that of GSDMB^{iso4}. The GSDMB^{iso1}-N domain is only structured to P215, and residues 216–220 along with the interdomain linker (including the exon-7-derived sequence) are disordered (Fig. 4f). α5 and the loop linking to β6 assume a more compact conformation to compensate for the loss of exon-6-derived structures (Fig. 4f). These differences explain why GSDMB^{iso1} and GSDMB^{iso2} lack pyroptosis-inducing activity.

Implications of isoform-specific activity

In view of the isoform differences, we examined the two recent studies reporting pyroptosis-null function of GSDMB[6,8] and found that a 411-residue isoform (not in the NCBI database) was used. This isoform, listed in the UniProt database (termed isoformU or GSDMB^{IsoU}), results from non-canonical splice junction processing. GSDMB^{IsoU} is closest to GSDMB^{iso4} but has a four-residue insertion followed by an asparagine-to-aspartate substitution of the first residue in the exon-6-encoded sequence (Extended Data Fig. 8c). The insertion did not affect cleavage by GZMA (Extended Data Fig. 8d) but should disrupt or heavily affect the β10 structure of the GSDMB-N domain, thus blocking oligomerization and pore assembly. Indeed, GSDMB^{IsoU}-N, compared with the GSDMB^{iso4}-N domain, showed strongly reduced liposome leakage activity and induced much less pyroptosis in 293T cells (Extended Data Fig. 8e,f). GSDMB^{iso4}-N had no bactericidal activity on *S. flexneri* (Extended Data Fig. 5d–f) and caused only subtle cytotoxicity when expressed in *E. coli* (Extended Data Fig. 8g). Accordingly, GZMA induced weak pyroptosis in GSDMB^{IsoU}-expressing 293T cells and H1299 cells (previously used to suggest pyroptosis deficiency in GSDMB[6]) (Fig. 5a and Extended Data Fig. 8h,i). Quantitatively, 27 times more GZMA was needed to induce the same level of pyroptosis in GSDMB^{IsoU}-expressing cells as in GSDMB^{iso3}-expressing cells (Extended Data Fig. 8j). In natural killer cell killing assays, GSDMB^{IsoU} expression in target cells conferred little pyroptosis, in contrast to GSDMB^{iso3} but echoing findings with GSDMB^{iso1} (Fig. 5b). Thus, GSDMB^{IsoU} has minimal pore-forming activity owing to interference with the GSDMB-N domain structure.

We analysed GSDMB isoforms endogenously expressed in various cancer cell lines (Fig. 5c). OE19 cells (oesophageal carcinoma) showed the highest proportion of GSDMB^{iso3} and GSDMB^{iso4} (about 40%), whereas OVCAR-5 cells (ovarian carcinoma) had the lowest percentage of the two pyroptosis-competent isoforms (<6% of total *GSDMB* transcripts) (Fig. 5d). Following GZMA action, more than 50% of OE19 cells underwent pyroptosis, whereas most OVCAR-5 cells remained alive (Fig. 5e,f). Interferon-γ (IFNγ) markedly stimulated *GSDMB* expression[3] in SW837 (colorectal adenocarcinoma), HT29 (colorectal adenocarcinoma), OE33 (oesophageal carcinoma) and HCC1954 (breast carcinoma) cells (Fig. 5c); the proportion of GSDMB^{iso3} and GSDMB^{iso4} transcripts rose to over 50% in HT29 and HCC1954 cells (Fig. 5d). Accordingly, stimulated cells became more sensitive to GZMA

(Fig. 5g). The extent of pyroptosis in these cells correlated with the expression of GSDMB^{iso3} and GSDMB^{iso4}. Notably, GSDMB^{IsoU} transcripts were only weakly detected in all these cell lines, regardless of IFNγ stimulation (Fig. 5d). These data highlight the functional importance of the isoform-dependent pore-forming activity of GSDMB, particularly in mediating lymphocyte cytotoxicity.

GSDMB expression was detected in primary human small intestinal mucosal and rectal epithelial cells, but not in gastric mucosal and colonic epithelial cells (Extended Data Fig. 8k). IFNγ and tumour necrosis factor α (TNF) but not lipopolysaccharide (LPS) upregulated *GSDMB* in rectal epithelial cells; IFNγ also showed an effect in colonic epithelial cells. GSDMB^{iso3} was the dominant isoform in small intestinal mucosal and rectal epithelial cells (the two active isoforms made up 75% of the total *GSDMB* transcripts), whereas GSDMB^{IsoU} was negligibly expressed (Extended Data Fig. 8l). The pattern was unaffected by IFNγ, TNF or LPS. In IFNγ-treated colonic epithelial cells, GSDMB^{iso3} and GSDMB^{iso4} represented over 38% of *GSDMB* transcripts (Extended Data Fig. 8l). As intestinal epithelia are primary targets of *S. flexneri* and other enteric pathogens, our data reiterate the pyroptosis function of GSDMB in the defence against enteric infections.

Discussion

Unlike other pyroptosis-blocking bacterial factors[24–27], *Shigella* IpaH7.8 directly targets gasdermin. We show that IpaH7.8-catalysed ubiquitination causes efficient degradation of both GSDMB and GSDMD, resolving the discrepancy[6,7]. Our structural study and a very recent one[28] both elucidate how IpaH7.8 uses its LRRs to recognize exclusively the pore-forming domain in GSDMB; such a mechanism also applies to GSDMD. Notably, the affinity of IpaH7.8 binding to GSDMB and GSDMD varies greatly, probably to fit the cognate ubiquitin-transfer kinetics (affected by the lysine availability in GSDMB and GSDMD). The two gasdermins function in distinct immune contexts; their degradation by IpaH7.8, which does not occur in mice, is proposed as the reason why *S. flexneri* only causes bacillary dysentery in humans[6,7]. Despite the fact that humans are more sensitive to *S. flexneri* than mice, the action of IpaH7.8 stresses the importance of pyroptosis in antibacterial defence.

We find that GSDMB isoforms produced by alternative splicing have full or no pyroptotic activity. The presence of exon-6-derived sequences in the GSDMB-N domain dictates the pore-forming activity. The cryo-EM structure of the GSDMB pore, in comparison with its autoinhibited structure, uncovers a key role of exon-6-derived structures for protomer oligomerization in pore assembly. This also explains the absence of pyroptotic activity in the non-canonical splicing isoform used in two recent studies[6,8]. The exon-6-derived structure is conserved in human gasdermins[22,23], which explains the fact that residues 1–240 of GSDMD represent its smallest active fragment[5,9]. We also find that the composition of GSDMB isoforms, varying greatly in different cells, determines pyroptosis onset and extent following GZMA action. Thus, regulating *GSDMB* splicing may have a role in cytotoxic-T-lymphocyte-mediated immunity. In tumours, whereas malignant cells tend to downregulate pyroptosis for immune evasion[3,29,30], *GSDMB* transcription is subject to upregulation by IFNγ and other factors[3]. Thus, determining the levels of pyroptosis-competent GSDMB isoforms in target tumours may better guide cancer immunotherapy.

Online content

Any methods, additional references, Nature Portfolio reporting summaries, source data, extended data, supplementary information, acknowledgements, peer review information; details of author contributions and competing interests; and statements of data and code availability are available at https://doi.org/10.1038/s41586-023-05872-5.

1. Broz, P., Pelegrin, P. & Shao, F. The gasdermins, a protein family executing cell death and inflammation. *Nat. Rev. Immunol.* **20**, 143–157 (2020).
2. Shi, J., Gao, W. & Shao, F. Pyroptosis: gasdermin-mediated programmed necrotic cell death. *Trends Biochem. Sci.* **42**, 245–254 (2017).
3. Zhou, Z. et al. Granzyme A from cytotoxic lymphocytes cleaves GSDMB to trigger pyroptosis in target cells. *Science* **368**, eaaz7548 (2020).
4. Kayagaki, N. et al. Caspase-11 cleaves gasdermin D for non-canonical inflammasome signalling. *Nature* **526**, 666–671 (2015).
5. Shi, J. et al. Cleavage of GSDMD by inflammatory caspases determines pyroptotic cell death. *Nature* **526**, 660–665 (2015).
6. Hansen, J. M. et al. Pathogenic ubiquitination of GSDMB inhibits NK cell bactericidal functions. *Cell* **184**, 3178–3191 (2021).
7. Luchetti, G. et al. *Shigella* ubiquitin ligase IpaH7.8 targets gasdermin D for degradation to prevent pyroptosis and enable infection. *Cell Host Microbe* **29**, 1521–1530 (2021).
8. Rana, N. et al. GSDMB is increased in IBD and regulates epithelial restitution/repair independent of pyroptosis. *Cell* **185**, 283–298 (2022).
9. Ding, J. et al. Pore-forming activity and structural autoinhibition of the gasdermin family. *Nature* **535**, 111–116 (2016).
10. Liu, Z. et al. Crystal structures of the full-length murine and human gasdermin D reveal mechanisms of autoinhibition, lipid binding, and oligomerization. *Immunity* **51**, 43–49 (2019).
11. Jorgensen, I. & Miao, E. A. Pyroptotic cell death defends against intracellular pathogens. *Immunol. Rev.* **265**, 130–142 (2015).
12. Man, S. M., Karki, R. & Kanneganti, T. D. Molecular mechanisms and functions of pyroptosis, inflammatory caspases and inflammasomes in infectious diseases. *Immunol. Rev.* **277**, 61–75 (2017).
13. Broz, P. & Dixit, V. M. Inflammasomes: mechanism of assembly, regulation and signalling. *Nat. Rev. Immunol.* **16**, 407–420 (2016).
14. Shi, J. et al. Inflammatory caspases are innate immune receptors for intracellular LPS. *Nature* **514**, 187–192 (2014).
15. Rathinam, V. A. K., Zhao, Y. & Shao, F. Innate immunity to intracellular LPS. *Nat. Immunol.* **20**, 527–533 (2019).
16. Liu, X. et al. Inflammasome-activated gasdermin D causes pyroptosis by forming membrane pores. *Nature* **535**, 153–158 (2016).
17. Das, S. et al. GSDMB induces an asthma phenotype characterized by increased airway responsiveness and remodeling without lung inflammation. *Proc. Natl Acad. Sci. USA* **113**, 13132–13137 (2016).
18. Panganiban, R. A. et al. A functional splice variant associated with decreased asthma risk abolishes the ability of gasdermin B to induce epithelial cell pyroptosis. *J. Allergy Clin. Immunol.* **142**, 1469–1478 (2018).
19. Wang, K. et al. Structural mechanism for GSDMD targeting by autoprocessed caspases in pyroptosis. *Cell* **180**, 941–955 (2020).
20. Rohde, J. R., Breitkreutz, A., Chenal, A., Sansonetti, P. J. & Parsot, C. Type III secretion effectors of the IpaH family are E3 ubiquitin ligases. *Cell Host Microbe* **1**, 77–83 (2007).
21. Kuang, S. et al. Structure insight of GSDMD reveals the basis of GSDMD autoinhibition in cell pyroptosis. *Proc. Natl Acad. Sci. USA* **114**, 10642–10647 (2017).
22. Ruan, J., Xia, S., Liu, X., Lieberman, J. & Wu, H. Cryo-EM structure of the gasdermin A3 membrane pore. *Nature* **557**, 62–67 (2018).
23. Xia, S. et al. Gasdermin D pore structure reveals preferential release of mature interleukin-1. *Nature* **593**, 607–611 (2021).
24. Kobayashi, T. et al. The *Shigella* OspC3 effector inhibits caspase-4, antagonizes inflammatory cell death, and promotes epithelial infection. *Cell Host Microbe* **13**, 570–583 (2013).
25. Chung, L. K. et al. The *Yersinia* virulence factor YopM hijacks host kinases to inhibit type III effector-triggered activation of the pyrin inflammasome. *Cell Host Microbe* **20**, 296–306 (2016).
26. Ratner, D. et al. The *Yersinia pestis* effector YopM inhibits pyrin inflammasome activation. *PLoS Pathog.* **12**, e1006035 (2016).
27. Li, Z. et al. *Shigella* evades pyroptosis by arginine ADP-riboxanation of caspase-11. *Nature* **599**, 290–295 (2021).
28. Yin, H. et al. Insights into the GSDMB-mediated cellular lysis and its targeting by IpaH7.8. *Nat. Commun.* **14**, 61 (2023).
29. Wang, Y. et al. Chemotherapy drugs induce pyroptosis through caspase-3 cleavage of a gasdermin. *Nature* **547**, 99–103 (2017).
30. Zhang, Z. et al. Gasdermin E suppresses tumour growth by activating anti-tumour immunity. *Nature* **579**, 415–420 (2020).

Methods

Plasmids

DNA encoding IpaH7.8 was amplified from the genomic DNA of *S. flexneri* 2457T. cDNAs for *GSDMB* isoforms were synthesized by our in-house gene synthesis facility. cDNAs for *GSDMA*, *GSDMC*, *GSDMD*, *GSDME* and mouse *Gsdmd* were described previously[3]. For stable expression in mammalian cells, cDNAs of GSDMB isoforms were inserted into the pLVX-IRES-Zsgreen1 lentiviral vector, and those bearing a PPase site were cloned into the FUIW-IRES-EGFP lentiviral vector. For transient transfection, cDNAs for *GSDMA*, *GSDMB*, *GSDMC*, *GSDMD*, *GSDME* and mouse *Gsdmd* were inserted into the pLVX-Flag-EGFP vector and DNA for IpaH7.8 was cloned into the FUIW-IRES-mCherry vector, with an N-terminal Flag and Myc tag, respectively. DNAs encoding the N-domains of the GSDMB isoforms were cloned into the pLVX-IRES-Zsgreen1 vector.

To examine cytotoxicity in *E. coli*, DNAs encoding the N-domains of the GSDMB isoforms were cloned into the pET21a vector; the start codon for the GSDMB^{iso4}-N domain was substituted with TTG to reduce background expression. For recombinant expression in *E. coli*, DNA for IpaH7.8 was cloned into the pGEX-6p-2 vector with an N-terminal glutathione *S*-transferase (GST) tag. DNAs for GSDMB isoforms were cloned into a modified pET vector with an N-terminal 6×His–maltose-binding protein (MBP) tag followed by a PPase site. DNAs for GSDMB isoforms and GSDMD bearing a PPase site, human and mouse GSDMD, GSDMB-C domain and GSDMD-C domain were cloned into the pSUMO vector with an N-terminal 6×His–SUMO tag. DNA for IpaH7.8^{LRR} was cloned into the pET28a vector for expression by itself and the pET21a vector for coexpression with GSDMB. All deletions, insertions and point mutations were generated by standard PCR cloning methods. All plasmids were verified by DNA sequencing.

Antibodies, compounds and reagents

Monoclonal antibody against human GSDMB (ab215729) and anti-Myc antibody (HX1821) were obtained from Abcam and Huaxing Bio, respectively. Antibodies against Flag (F3165/M2) and tubulin (T5168) were purchased from Sigma-Aldrich. Horseradish peroxidase (HRP)-conjugated anti-mouse IgG (NA931) and HRP-conjugated anti-rabbit IgG (NA934) were purchased from GE Healthcare.

IFNγ (285-IF-100) was purchased from R&D, and calcein AM (C1430) was from ThermoFisher Scientific. LMNG (NG310) was purchased from Anatrace. Natural and synthetic lipid products used for liposome preparation were from Avanti Polar Lipids, including 1-palmitoyl-2-oleoyl-glycero-3-phosphocholine (POPC, 850457), 1-palmitoyl-2-oleoyl-*sn*-glycero-3-phosphate (POPA, 840857), 1,2-dioleoyl-*sn*-glycero-3-phosphoethanolamine (DOPE, 850725), 1-palmitoyl-2-oleoyl-*sn*-glycero-3-phospho-L-serine (POPS, 840034), liver L-α-phosphatidylinositol (PI, 840042), 1′,3′-bis[1,2-dioleoyl-*sn*-glycero-3-phospho]-glycerol (cardiolipin, 710335) and brain L-α-phosphatidylinositol-4,5-bisphosphate (PI(4,5)P_2, 840046). LPS (L4130), terbium chloride ($TbCl_3$, 212903) and DPA (P63808) were obtained from Sigma-Aldrich.

Cell culture, transfection and electroporation

HEK293T, OVCAR-5, HT29 and COLO 205 cells were obtained from the American Type Culture Collection (ATCC). Primary epithelial cells were obtained from iCell Bioscience. OE19, HCC1954 and OE33 cells were purchased from Cobioer. H1299 cells were a gift from X. Wang (National institute of Biological Sciences, Beijing). SW837 cells were provided by X. Zhao (Air Force Medical University, China). NK-92MI cells were a gift from Z. Shen (BeiGene). HEK293T and SW837 cells were grown in DMEM supplemented with 10% (v/v) FBS, 2 mM L-glutamine, 100 mg ml^{-1} penicillin and 100 mg ml^{-1} streptomycin. OVCAR-5, COLO 205, OE33, HT29, OE19, HCC1954 and H1299 cells were grown in RPMI-1640 supplemented with 10% (v/v) FBS, 2 mM L-glutamine, 100 mg ml^{-1} penicillin and 100 mg ml^{-1} streptomycin. NK-92MI cells were grown in α-MEM supplemented with 0.2 mM inositol, 0.1 mM 2-mercaptoethanol, 0.02 mM folic acid, 10 mM HEPES, 1× non-essential amino acids (NEAAs) (Life Technologies), 20% (v/v) FBS, 100 mg ml^{-1} penicillin and 100 mg ml^{-1} streptomycin. Primary gastrointestinal epithelial cells were grown in commercial iCell Primary Epithelial Cell Medium from iCell Bioscience.

Transient transfection was performed using jetPRIME (Polyplus-transfection) following the manufacturer's instructions. For stable expression, lentiviral plasmids harbouring the desired gene were transfected into 293T cells together with the packaging plasmids psPAX2 and pMD2G at a ratio of 5:3:2. The supernatants were collected 48 h after transfection and used to infect 293T or H1299 cells for another 24 h. The infected EGFP-positive cells were sorted by flow cytometry using a FACSAria II (BD Biosciences). Electroporation of recombinant proteins into mammalian cells was carried out using the NeonTransfection System (ThermoFisher Scientific) following the manufacturer's instructions. In brief, cells were prepared at a final density of about 1×10^7 cells per ml. Then, 100 µl of cells was mixed with 1.5 µg of homemade CASP4-p20/p10, 20 µg of GZMA or 60 µg of PPase, and electroporation was carried out using the following parameters: 1,250 V, 10 ms, 2 pulses.

Immunoprecipitation, cell viability and cytotoxicity

For immunoprecipitation, 293T cells grown to 75% confluence were transfected with the indicated plasmids. Twenty-four hours later, cell pellets were collected and lysed in lysis buffer (50 mM Tris-HCl pH 8.0, 150 mM NaCl, 2 mM EDTA, 1% (v/v) Triton X-100 and protease inhibitor cocktail) for 0.5 h followed by centrifugation at 4 °C (15,000 r.p.m. for 10 min). The lysates were incubated with anti-Flag M2 affinity beads at 4 °C with gentle rotation for 2 h. The beads were washed five times with lysis buffer, and the immunoprecipitates were eluted with SDS loading buffer and then denatured at 95 °C for 15 min. The samples were applied to standard immunoblotting.

Cell viability was determined with the CellTiter-Glo Luminescent Cell Viability Assay (Promega). Cell cytotoxicity was measured by LDH release assay using the CytoTox 96 Non-Radioactive Cytotoxicity Assay kit (Promega).

Natural killer cell killing assays

Natural killer cell killing assays were performed as previously described[3]. In brief, 1×10^6 target cells were preloaded with 4 µg ml^{-1} calcein AM in 1 ml of complete medium at 37 °C for 30 min. The cells were then washed twice with PBS and suspended in 5 ml of NK-92MI medium. NK-92MI cells were co-cultured with the target cells for 6 h, and the effector/target cell (E/T) ratio was 8 in a 96-well plate. Live target cells without co-culturing with NK-92MI cells were used to determine the spontaneous (basal) and maximal release of calcein. Fluorescence of the released calcein was measured by using an excitation wavelength of 485 nm and an emission wavelength of 530 nm. The percentage of calcein release, indicative of the extent of target cell death, was calculated as follows: (calcein release determined from the killing assay − basal release)/(maximal calcein release − basal release).

Quantification of *GSDMB* isoform expression

RNAs in the indicated cell lines were extracted using the FastPure Cell/Tissue Total RNA Isolation Kit V2 (Vazyme), and first-strand cDNA was synthesized using the All-In-One 5X RT MasterMix kit (Applied Biological Materials). The common region of *GSDMB* isoforms was amplified using the following primers: forward, 5′-AATGATACGGCGACCACCGAGATCTACACTCTTTCCCTACACGACGCTCTTCCGATCTCTTGTCTTCCCCAACAAGGAG-3′; reverse, 5′-CAAGCAGAAGACGGCATACGAGAT<u>NNNNNN</u>GTGACTGGAGTTCAGACGTGTGCTCTTCCGATCGAAATCAGGACCTCAGATACTC-3′ (the underlined sequence was the index for individual samples). The PCR products were subjected to electrophoresis on a 2% agarose gel, and DNA bands were excised and sequenced on the HiSeq 2500 platform (Illumina).

Bacterial growth inhibition assays

To examine the cytotoxicity of the GSDMB-N domain in bacteria, equal numbers of *E. coli* BL21 (DE3) pLysS competent cells were transformed with 0.1 μg of the indicated plasmids. Cells were serially diluted and plated onto LB agar with ampicillin and chloramphenicol in the presence or absence of isopropyl β-D-1-thiogalactopyranoside (IPTG). Colony-forming units (CFUs) were determined by counting the number of viable bacteria per transformation after overnight culture at 37 °C.

To examine the bactericidal activity of the GSDMB isoforms, *S. flexneri* 2a strain 2457T was grown overnight in BHI medium and diluted 1:200 in BHI followed by growth for another 3 h at 37 °C to obtain log-phase culture. Then, 1 ml of the culture was centrifuged at 4,000 r.p.m. for 2 min, washed once in TBS (50 mM Tris pH 8.0 and 150 mM NaCl) and resuspended in TBS at 1×10^9 cells per ml. Reaction aliquots of 15 μl were set up in TBS by mixing 64 mM of the $GSDMB^{PP}$ isoforms with 6.4 mM PPase. TBS, $GSDMB^{PP}$ and PPase alone were assayed as controls. Five microlitres of the log-phase culture (5×10^6 cells) was immediately added to each reaction, and reactions were incubated for 2 h at 37 °C. Serial dilutions were plated on BHI agar to determine CFUs.

Recombinant protein expression and purification

The *E. coli* BL21 (DE3) strain was used for recombinant protein expression. Bacteria harbouring the desired expression plasmids were cultured in LB with the appropriate antibiotics. Expression of all target proteins except for $IpaH7.8^{LRR}$ was induced with 0.4 mM IPTG at 20 °C for 20 h after the OD_{600} reached 0.8. Specifically, IpaH7.8 proteins were purified by glutathione affinity chromatography in buffer A containing 200 mM NaH_2PO_4/K_2HPO_4 (pH 7.4), 137 mM NaCl, 2.7 mM KCl, 10% glycerol and 2 mM β-mercaptoethanol. The GST tag was removed by overnight digestion with homemade PPase at 4 °C. The tag-removed proteins were further purified by HiTrap Q HP anion-exchange chromatography and Superdex G75 gel-filtration chromatography and then concentrated and stored in buffer B containing 200 mM NaH_2PO_4/K_2HPO_4 (pH 7.4), 137 mM NaCl, 2.7 mM KCl and 1 mM Tris(2-carboxyethyl)-phosphine hydrochloride (TCEP). To prepare biotinylated IpaH7.8 protein for SPR measurements, the 15-residue Avi tag was inserted upstream of the N terminus of IpaH7.8, and the tagged IpaH7.8 construct was coexpressed with *E. coli* biotin ligase (BirA) in BL21 (DE3) cells. The purification process followed that for the unmodified IpaH7.8, and the modification efficiency was checked by anti-biotin immunoblotting.

Expression of $IpaH7.8^{LRR}$ in the pET28a vector was induced with 0.2 mM IPTG at 16 °C for 20 h after the OD_{600} reached 0.6. 6×His-tagged $IpaH7.8^{LRR}$ was purified by nickel affinity chromatography in buffer C containing 200 mM NaH_2PO_4/K_2HPO_4 (pH 6.8), 600 mM NaCl, 2.7 mM KCl, 7% glucose and 2 mM β-mercaptoethanol. $IpaH7.8^{LRR}$ was eluted from the nickel affinity beads using buffer C supplemented with 500 mM imidazole and further purified by HiTrap Q HP anion-exchange chromatography followed by Superdex G75 gel-filtration chromatography. Purified $IpaH7.8^{LRR}$ was stored in buffer D containing 200 mM NaH_2PO_4/K_2HPO_4 (pH 6.8), 600 mM NaCl, 2.7 mM KCl and 2 mM dithiothreitol (DTT).

To purify GSDMB isoforms inserted with or without a PPase site (point mutants were on the isoform 4 background), 6×His–MBP- or 6×His–SUMO-tagged GSDMB proteins were purified by nickel affinity chromatography in buffer E containing 20 mM Tris-HCl (pH 8.0), 300 mM NaCl and 20 mM imidazole; the MBP and SUMO tags were removed by overnight digestion at 4 °C with homemade His–PPase and ULP1, respectively. The tag-removed proteins were further purified by HiTrap Q HP anion-exchange and Superdex G75 gel-filtration chromatography. The purification process for the GSDMB-C domain was identical to that for 6×His–SUMO–GSDMB proteins. Expression and purification of human and mouse GSDMD and GSDMD-C domain were performed as previously described[19]. Purified gasdermin proteins were stored in buffer F containing 20 mM Tris-HCl (pH 8.0) and 150 mM NaCl.

To obtain GSDMB–$IpaH7.8^{LRR}$ complex for crystallization, 6×His–MBP-tagged GSDMB isoform 1 (with residues 68–80 deleted) or isoform 4 was coexpressed with untagged $IpaH7.8^{LRR}$ in BL21 (DE3) cells. The purification process was the same as that for GSDMB alone. The purified GSDMB–$IpaH7.8^{LRR}$ complex was stored in buffer F. To assay binding of paired proteins, purified proteins were incubated at a molar ratio of 1:1 for 2 h on ice and the mixtures were then loaded onto a Superdex 200 Increase 10/300 GL column and eluted with buffer F. Each isolated protein was analysed on the same column as controls. The eluted fractions were subjected to SDS–PAGE analyses.

Crystal structure determination

Crystallization experiments were carried out at 20 °C using the sitting-drop vapour diffusion method by mixing 1 μl of protein solution with 1 μl of reservoir solution. Initial crystallization screening was performed by using commercial kits (Hampton Research). Qualified crystals of $GSDMB^{iso4}$–$IpaH7.8^{LRR}$ were obtained in reservoir buffer containing 1.2 M NaH_2PO_4/K_2HPO_4 (pH 7.2). Crystals of $GSDMB^{iso1}$–$IpaH7.8^{LRR}$ were obtained from reservoir buffer containing 0.1 M Li_2SO_4, 0.6 M $(NH_4)H_2PO_4$ and 0.1 M sodium acetate (pH 4.6).

All crystals were transferred to a cryoprotectant solution containing reservoir buffer supplemented with 15% (v/v) ethylene glycol or glycerol before flash-freezing with liquid nitrogen. Diffraction data were collected at the Shanghai Synchrotron Radiation Facility (Shanghai, China) beamline BL19U1 and SPring-8 (Hyogo, Japan) beamline BL45XU and processed with the XDS package[31]. The phase of both structures was determined by the molecular replacement method using the GSDMB and $IpaH7.8^{LRR}$ structures predicted by AlphaFold[32] as initial models; automatic model building was performed in the PHENIX suite[33]. The rest of the model was manually built in Coot[34]. All structures were refined in PHENIX, and manual modelling was performed between refinement cycles. The statistics of data collection and refinement are summarized in Extended Data Table 1. The quality of the final models was validated by MolProbity[35]. All structural figures were prepared in PyMOL or ChimeraX[36].

SPR assays

SPR experiments were carried out at 12 °C in filtered and degassed running buffer containing 200 mM NaH_2PO_4/K_2HPO_4 (pH 7.4), 137 mM NaCl, 2.7 mM KCl, 1 mM TCEP and 0.1% (w/v) Pluronic F-127 by using a Biacore 8K SPR instrument (Cytiva). Specifically, the flow cells of a streptavidin (SA) sensor chip (Cytiva) were pretreated with three consecutive 1-min injections of buffer containing 1 M NaCl and 50 mM NaOH at a flow rate of 10 μl min^{-1}. IpaH7.8 protein was diluted in running buffer to a concentration of 50 μg ml^{-1} and immobilized on the SA chip to a response signal of 5,500 units. The SA chip with captured proteins was then washed with buffer containing 50% isopropanol, 1 M NaCl and 50 mM NaOH at a flow rate of 10 μl min^{-1}.

The indicated GSDMB or GSDMD proteins at a series of concentrations were injected into the flow cells to pass over the immobilized IpaH7.8. The titrating protein concentrations were 0.05 μM, 0.15 μM, 0.45 μM, 1.35 μM, 4.05 μM and 12.15 μM for GSDMB, 0.56 μM, 1.67 μM, 5 μM, 15 μM, 45 μM and 135 μM for GSDMD and 1.2 μM, 3.59 μM, 10.77 μM, 32.3 μM and 96.9 μM for mouse GSDMD. The binding signals of GSDMB were measured by a single-cycle method with 120-s association and 600-s dissociation at a flow rate of 30 μl min^{-1}, whereas those of human and mouse GSDMD were measured by a multiple-cycle method with 120-s association and 240-s dissociation at a flow rate of 30 μl min^{-1}. The data were fitted to a 1:1 binding mode using the program provided by the manufacturer. The binding constant (K_d) was calculated directly from the fitting.

Liposome leakage assays

Tb^{3+}-encapsulated liposomes with the indicated phospholipid compositions were prepared by following a previously described protocol[9].

Aliquots of the liposomes were diluted to a lipid concentration of 300 μM in 90 μl of buffer G containing 20 mM HEPES (pH 7.5) and 150 mM NaCl supplemented with 15 μM DPA. DPA chelates of Tb^{3+} released from the liposomes were excited at a wavelength of 270 nm, and the emission wavelength was 490 nm. The emission fluorescence before addition of protein samples was treated as Ft_0. Ten microlitres of GSDMB proteins and PPase were added to a final concentration of 0.6 μM and 0.15 μM, respectively, and the emission fluorescence was continuously recorded as Ft at 15-s intervals. After 40 min, 10 μl of 1% (v/v) Triton X-100 was added to achieve complete release of Tb^{3+}, and the mean values of the top three fluorescence reads were defined as Ft_{100}. The percentage of liposome leakage at each time point was determined as leakage (t) (%) = $(Ft - Ft_0) \times 100/(Ft_{100} - Ft_0)$.

Reconstitution of GSDMB pores

POPC, POPA and cardiolipin dissolved in chloroform were mixed in a glass tube at a molar ratio of 3:1:1, and the solvent was evaporated under a stream of nitrogen gas. The dry lipid film was hydrated at room temperature with constant mixing in buffer H containing 20 mM Tris-HCl (pH 8.0), 150 mM NaCl and 5 mM DTT, to yield a lipid suspension (lipid concentration, 2.5 mM). Liposomes were generated by extrusion of the hydrated lipids through a 100-nm polycarbonate filter (Whatman) 31 times using the Mini-Extruder device (Avanti Polar Lipids). To prepare GSDMB pores, purified $GSDMB^{iso4}$ containing a PPase site and homemade PPase were incubated together with the liposomes for 1.5 h at room temperature. The perforated liposomes were collected by ultracentrifugation at 60,000*g* for 30 min at 4 °C and solubilized by buffer H supplemented with 0.5% (w/v) LMNG. After a new round of centrifugation at 13,000*g* for 10 min at 4 °C, the supernatants containing extracted GSDMB pores were further purified on a Superose 6 gel-filtration column (Cytiva) equilibrated with buffer H containing 0.005% (w/v) LMNG. The pore concentration for EM sample preparation was about 0.1 mg ml^{-1}.

Negative-stain EM

For negative-stain EM, 5 μl of purified GSDMB pores was transferred onto glow-discharged EM copper grids coated with a layer of lacey carbon support film (Zhongjingkeyi Co.). The grids were then washed several times with water to remove the detergents and negatively stained with 2% uranyl acetate for 30 s followed by air drying. The grids with captured GSDMB pores were imaged on a Tecnai T12 microscope (FEI) at 120 kV. Images were taken on a Gatan 4k × 4k CCD camera with a nominal magnification of ×30,000, giving a final pixel size of 3.71 Å.

Cryo-EM data collection

A 2.5-μl aliquot of purified GSDMB pores was applied to a glow-discharged GraFuture-GO grid (Shuimu Biosciences), blotted with filter paper for 1 s and then plunge-frozen in liquid ethane using a Vitrobot Mark IV cryo-EM system (ThermoFisher). Cryo-EM data were collected on a 300-kV Titan Krios G3i electron microscope (ThermoFisher) equipped with a Gatan K3 direct detection camera. Micrographs were collected in counting mode at a calibrated magnification of ×53,000, yielding a pixel size of 1.08 Å. A total of 7,989 micrographs were obtained, each of which was exposed with an accumulated dose of 50 electrons per $Å^2$ per second and fractionated into a stack of 32 frames with a defocus range of −1.0 to −2.0 μm.

Cryo-EM image processing and model building

Beam-induced motion correction was performed on the stack of frames using MotionCorr2 (ref. [37]). The contrast transfer function (CTF) parameters were determined with CTFFIND4 (ref. [38]). A total of 7,790 good micrographs were selected for further processing using the cryoSPARC software suite[39]. Particles were auto-picked with the program Blob-picker, followed by reference-free 2D classification with different parameter adjustments. Next, particle selection was performed using the program Template-picker with the best 11 2D classes from the last step as templates and simultaneously tested using Blob-picker with modified parameters. Following particle selection, another four rounds of 2D classification were performed. A total of 1,990,948 particles were selected from good 2D classes and subjected to 3D ab initio reconstruction to obtain an initial 3D model. To ensure accurate symmetry of the GSDMB pore, several rounds of parameters were tested; the 3D classifications indicated that the GSDMB pore has heterogenous symmetry, including C_{26}, C_{27} and C_{28}, among which the C_{27} class is the dominant one. The C_{27} class was subjected to structural determination, and the best particles selected from 2D classification were subjected to four rounds of 3D classification by using the program Heterogeneous Refinement with a 27-fold starting model as a reference. However, most of the particles selected from the 2D or 3D classifications were top views that caused severe orientation preference in 3D reconstruction. To circumvent this issue, the side and top views of the pores were manually separated through two more rounds of 2D classification. The C_{27} class of top view particles were combined with all the best side view particles for one more round of 3D refinement. Finally, the 3D GSDMB pore structure with C_{27} symmetry was reconstructed from 85,337 particles at a global resolution of 3.17 Å based on the gold-standard Fourier shell correlation criterion of FSC = 0.143 after symmetry-imposed refinement and CTF refinement. The local resolution was calculated from the final density map. The model of the GSDMB pore was built by fitting the structure of the GSDMB-N domain in full-length GSDMB into the density map using ChimeraX[36], followed by manual building in Coot[34] and refinement in PHENIX[33]. The model statistics are listed in Extended Data Table 2.

Statistics and reproducibility

Information concerning statistics and reproducibility for the experiments in this study is given in the figure legends for the corresponding experiments.

Reporting summary

Further information on research design is available in the Nature Portfolio Reporting Summary linked to this article.

Data availability

The atomic coordinates and structure factors generated in this study have been deposited in PDB under accession codes 8GTJ, 8GTK and 8GTN. The following PDB entries were used in this study: 6N9O, 5B5R, 6VFE and 6CB8. Source data are provided with this paper.

Code availability

No custom code was used in this work.

31. Kabsch, W. Xds. *Acta Crystallogr. D* **66**, 125–132 (2010).
32. Jumper, J. et al. Highly accurate protein structure prediction with AlphaFold. *Nature* **596**583–589 (2021).
33. Liebschner, D. et al. Macromolecular structure determination using X-rays, neutrons and electrons: recent developments in Phenix. *Acta Crystallogr. D* **75**, 861–877 (2019).
34. Emsley, P., Lohkamp, B., Scott, W. G. & Cowtan, K. Features and development of Coot. *Acta Crystallogr. D* **66**, 486–501 (2010).
35. Williams, C. J. et al. MolProbity: more and better reference data for improved all-atom structure validation. *Protein Sci.* **27**, 293–315 (2018).
36. Pettersen, E. F. et al. UCSF ChimeraX: structure visualization for researchers, educators, and developers. *Protein Sci.* **30**, 70–82 (2021).
37. Zheng, S. Q. et al. MotionCor2: anisotropic correction of beam-induced motion for improved cryo-electron microscopy. *Nat. Methods* **14**, 331–332 (2017).
38. Rohou, A. & Grigorieff, N. CTFFIND4: fast and accurate defocus estimation from electron micrographs. *J. Struct. Biol.* **192**, 216–221 (2015).
39. Punjani, A., Rubinstein, J. L., Fleet, D. J. & Brubaker, M. A. cryoSPARC: algorithms for rapid unsupervised cryo-EM structure determination. *Nat. Methods* **14**, 290–296 (2017).

Acknowledgements We thank the staff of beamline BL19U1 at the National Center for Protein Science (Shanghai) and the Shanghai Synchrotron Radiation Facility and beamline BL45XU at

SPring-8 (Hyogo, Japan) for assistance with X-ray data collection, X. Ni (Shuimu BioSciences Co. Ltd) for assistance with cryo-EM data collection and the staff of the Sequencing Center and the EM Center at the National Institute of Biological Sciences, Beijing, for quantitative DNA sequencing and checking EM samples. This work was supported by the National Key R&D Program of China (2022YFA1304700), the Chinese Academy of Medical Sciences Innovation Fund for Medical Sciences (2019-I2M-5-084), the CAS Strategic Priority Research Program (XDB29020202 and XDB37030202), the Basic Science Center Project (81788104) and Excellent Young Scholar Program (81922043) of NSFC, and a grant from the Youth Innovation Promotion Association of CAS. F.S. is also supported by the Tencent New Cornerstone Investigator Program.

Author contributions J.D. and F.S. conceived and supervised the study; X.Z. determined the crystal structures and performed biochemical assays; H.Z. reconstituted GSDMB pores for EM analyses and also performed in vitro liposome assays; Z.Z. contributed all the cellular data; Y. Su made the initial observation of isoform-dependent function of GSDMB; H.C. processed the cryo-EM data and generated the density map; Y.H. assisted H.Z. in cryo-EM data collection and built and refined the pore structure; Y. She, N.F. and J.W. provided technical assistance; and J.D. and F.S. analysed the data and wrote the manuscript. All authors discussed the results and commented on the manuscript.

Competing interests The authors declare no competing interests.

Additional information

Supplementary information The online version contains supplementary material available at https://doi.org/10.1038/s41586-023-05872-5.

Correspondence and requests for materials should be addressed to Feng Shao or Jingjin Ding.

Peer review information *Nature* thanks the anonymous reviewers for their contribution to the peer review of this work.

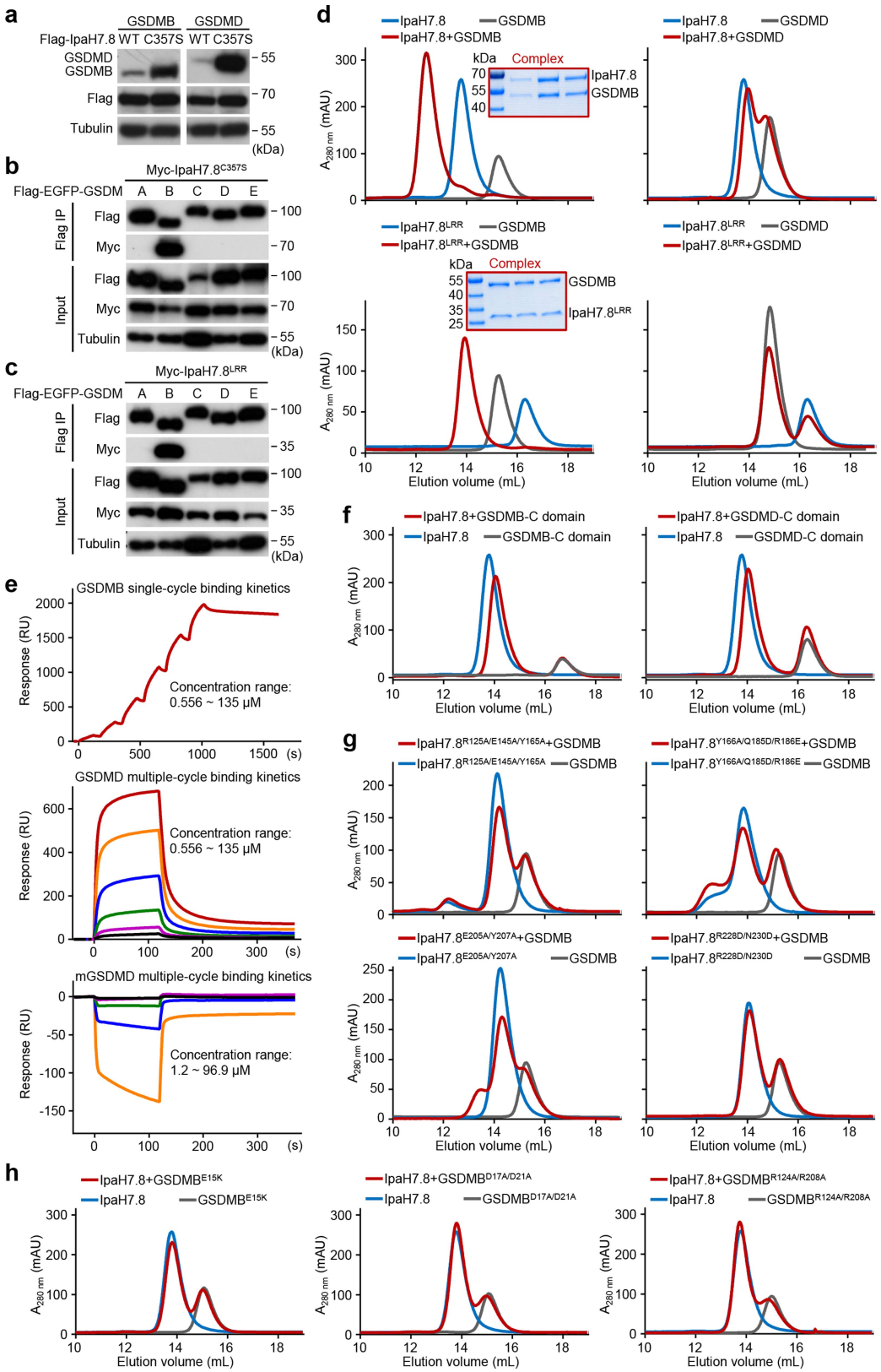

Extended Data Fig. 1 | See next page for caption.

Extended Data Fig. 1 | Biochemical characterization of IpaH7.8–GSDMB interaction. a, Assay of GSDMB (or GSDMD) degradation by IpaH7.8. Flag-IpaH7.8 (WT or C357S) was co-expressed with GSDMB or GSDMD in 293T cells. Cell lysates were subjected to immunoblotting analyses. **b**, **c**, Co-immunoprecipitation assay of IpaH7.8 with human gasdermins (GSDMs). IpaH7.8^{C357S} mutant (**b**) or IpaH7.8^{LRR} (**c**) was co-expressed with an indicated Flag-EGFP-tagged GSDM in 293T cells. Cell lysates were subjected to anti-Flag immunoprecipitation followed by immunoblotting. **d**, **f**, Gel-filtration chromatography analyses of complex formation between IpaH7.8 or IpaH7.8^{LRR} and GSDMB or GSDMD (FL or the C-terminal domain). Elution profiles along with SDS-PAGE analyses of complex elution fractions are shown. **e**, SPR profiles of IpaH7.8 binding to GSDMB or human or mouse GSDMD. **g**, **h**, Gel-filtration chromatography analyses of complex formation between IpaH7.8 (WT or indicated GSDMB-binding site mutants) and GSDMB (WT or indicated IpaH7.8-binding site mutants). The binding-site mutations in IpaH7.8 and GSDMB were identified from the complex crystal structure. All data are representative of three independent experiments. See Supplementary Fig. 1 for gel source data.

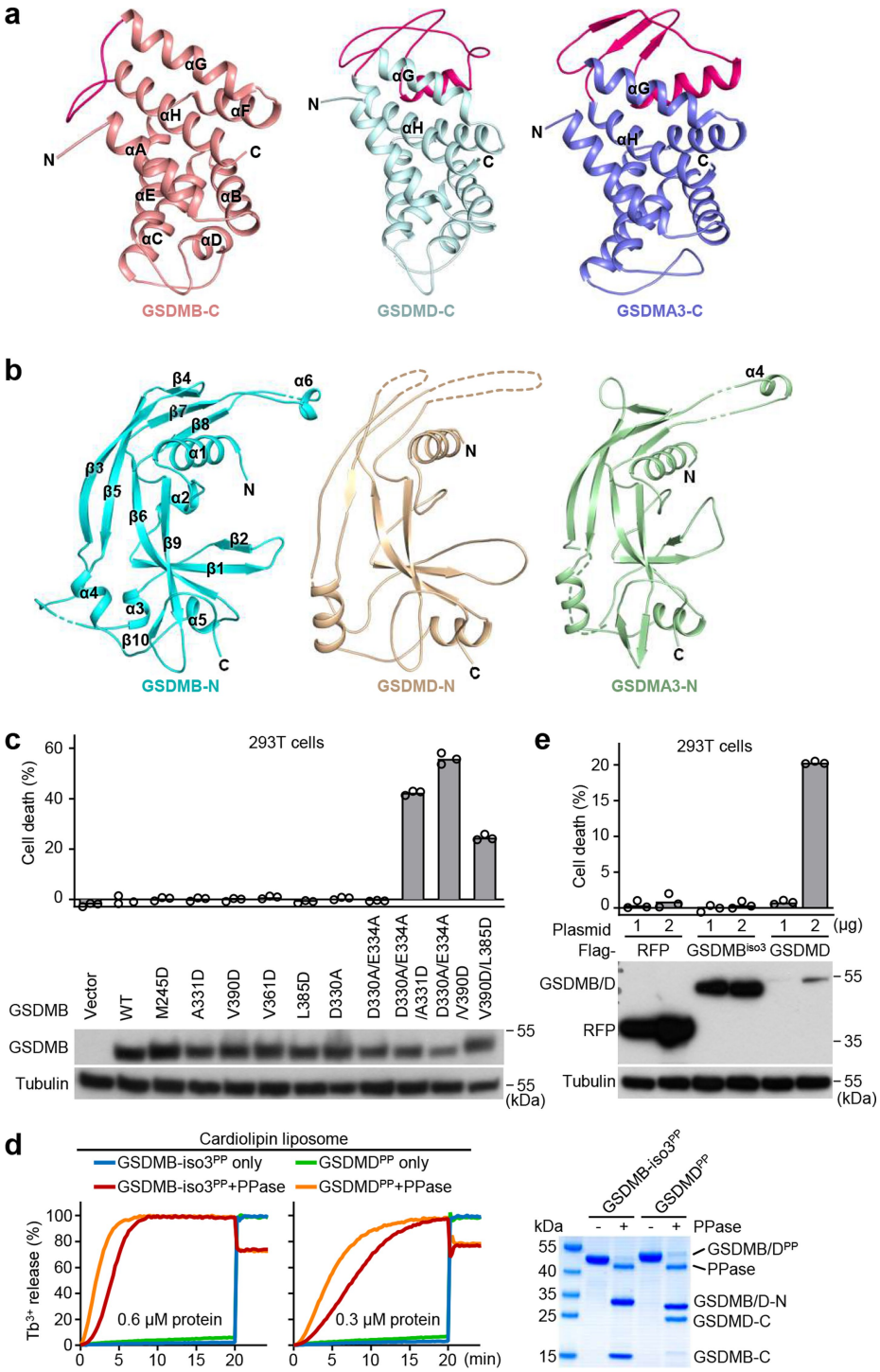

Extended Data Fig. 2 | Structural and functional analyses of the autoinhibition of GSDMB. a, **b**, Domain structural comparisons of GSDMB with other gasdermins. **a**, **b**, Cartoon structural models of the GSDMB-C domain (**a**) and the GSDMB-N domain (**b**) (second structural elements numbered) are compared with their counterparts in GSDMD (PDB: 6N9O) or mouse GSDMA3 (PDB: 5B5R). **a**, The linker regions between αG and αH in the three domains are highlighted. **c**, Mutagenesis analyses of the interdomain autoinhibition of GSDMB. GSDMB (WT or an indicated mutant to disrupt the autoinhibition) was transfected into 293T cells. Expression of the transfected GSDMB was examined by immunoblotting analyses. LDH release-based cell death data are means (bars) of three replicates (circles). **d**, Comparison of GSDMD and GSDMB liposome-leakage activity. Cardiolipin liposomes were treated with 0.6 or 0.3 μM purified GSDMB^{PP} (isoform 3) or GSDMD^{PP} in the presence or absence of PPase. Liposome leakage was monitored by measuring DPA chelating-induced fluorescence of the released Tb^{3+}. Cleavage of GSDMB^{PP} and GSDMD^{PP} by PPase was analyzed by SDS-PAGE. **e**, Comparison of basal pyroptotic activity in FL GSDMB and GSDMD. Indicated amounts of GSDMB or GSDMD plasmid were transiently overexpressed in 293T cells. LDH release-based cell death data are means (bars) of three replicates (circles). Expression of the transfected constructs was examined by immunoblotting. Data (**c**–**e**) are representative of three independent experiments. See Supplementary Fig. 1 for gel source data.

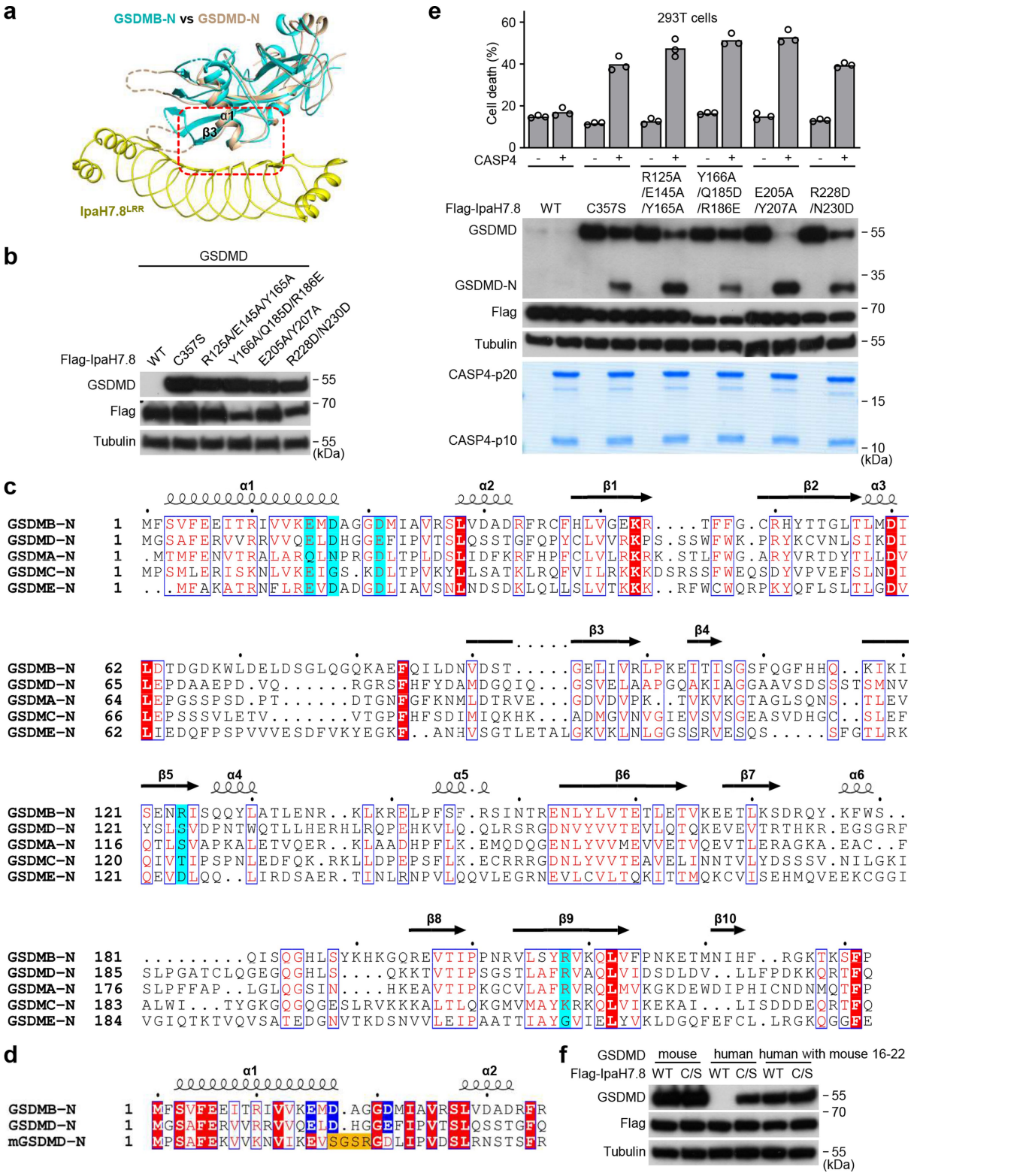

Extended Data Fig. 3 | See next page for caption.

Extended Data Fig. 3 | Structural and functional analyses of IpaH7.8 recognition of GSDMD. a, Structural modeling of IpaH7.8 recognition of GSDMD. Structure of GSDMD-N domain from FL GSDMD (PDB: 6N9O) is overlaid with that of GSDMB-N domain (from the IpaH7.8^{LRR}–GSDMB complex). The binding interface is highlighted by a red box with structural elements labeled. **b**, Analyses of GSDMD degradation by IpaH7.8 mutants deficient in recognizing GSDMB. Flag-IpaH7.8 (WT, C357S, or a binding-site mutant) was co-expressed with GSDMD in 293T cells. Cell lysates were subjected to immunoblotting. **c**, **d**, Alignment of the N-terminal domain sequences of human gasdermins and mouse GSDMD. Second structural elements of GSDMB-N domain are numbered and shown on top of the sequences. Numbers of starting residues are indicated on the left. Identical residues are in red background and conserved ones are in red. Residues involved in binding IpaH7.8 are highlighted in cyan (**c**) or blue background (**d**). **e**, Functional validation of IpaH7.8 mutants in blocking GSDMD-mediated pyroptosis. Flag-IpaH7.8 (WT or an indicated mutant) and GSDMD were co-transfected into 293T cells and active CASP4 p20/p10 proteins were electroporated into the cells to induce GSDMD-dependent pyroptosis. IpaH7.8-induced degradation and CASP4 cleavage of GSDMD were examined by immunoblotting. SDS-PAGE analyses show the loading of CASP4 p20/p10 proteins. LDH release-based cell death data are means (bars) of three replicates (circles). **f**, Assay of mouse GSDMD degradation by IpaH7.8. Flag-IpaH7.8 (WT or C357S) was co-expressed in 293T cells with human or mouse GSDMD or human GSDMD with its L16–E21 sequences substituted with the mouse sequences (V16–D22). Cell lysates were subjected to immunoblotting. Data (**b**, **e**, **f**) are representative of three independent experiments. See Supplementary Fig. 1 for gel source data.

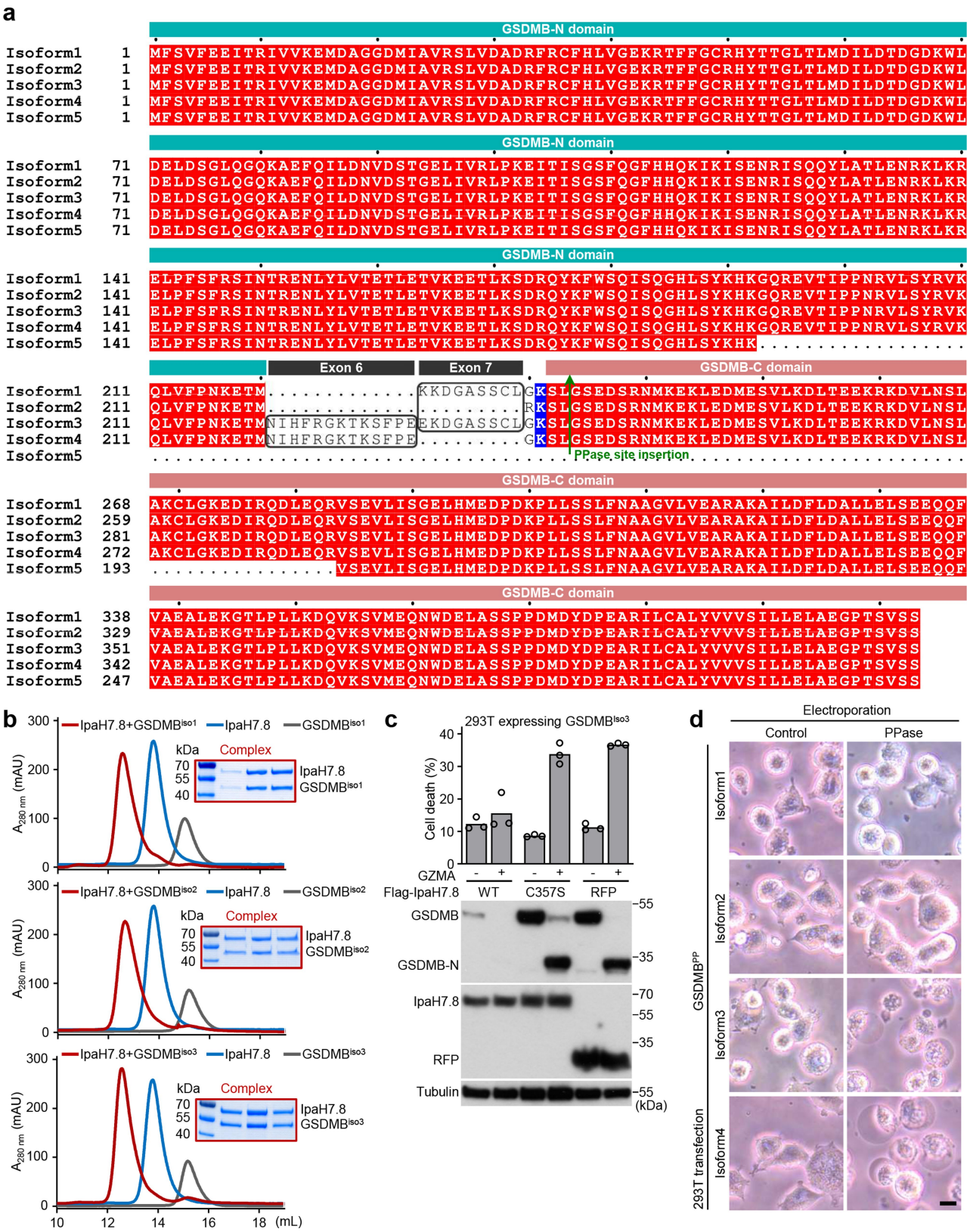

Extended Data Fig. 4 | See next page for caption.

Extended Data Fig. 4 | Sequence differences in GSDMB isoforms and characterizations of their functions. a, Sequence alignment of GSDMB isoforms. Domain annotation is shown on top of the sequences. The exon 6 and 7 regions are labeled and highlighted by black boxes. GZMA cleavage site Lys244 (numbered after GSDMB^{iso3}) is highlighted in blue background. The site for inserting a PPase-cleavage sequence is marked by a green arrow. Identical residues are in red background. Numbers of starting residues are indicated on the left. **b**, Gel-filtration chromatography analyses of complex formation between IpaH7.8 and different GSDMB isoforms, along with SDS-PAGE of the complex elution fractions. **c**, Assay of GSDMB^{Iso3} in IpaH7.8 blocking of GZMA-induced pyroptosis. Flag-IpaH7.8 (WT or C357S) was transfected into 293T cells stably expressing GSDMB^{Iso3}; GZMA was electroporated into the cells. LDH release-based cell death data are means (bars) of three replicates (circles). Cell lysates were subjected to immunoblotting. **d**, 293T cells expressing different GSDMB^{PP} isoforms were electroporated with PPase to cleave the GSDMB^{PP}. Morphological examination of cell pyroptosis is shown. Scale bar, 25 μm. Data (**b**–**d**) are representative of three independent experiments. See Supplementary Fig. 1 for gel source data.

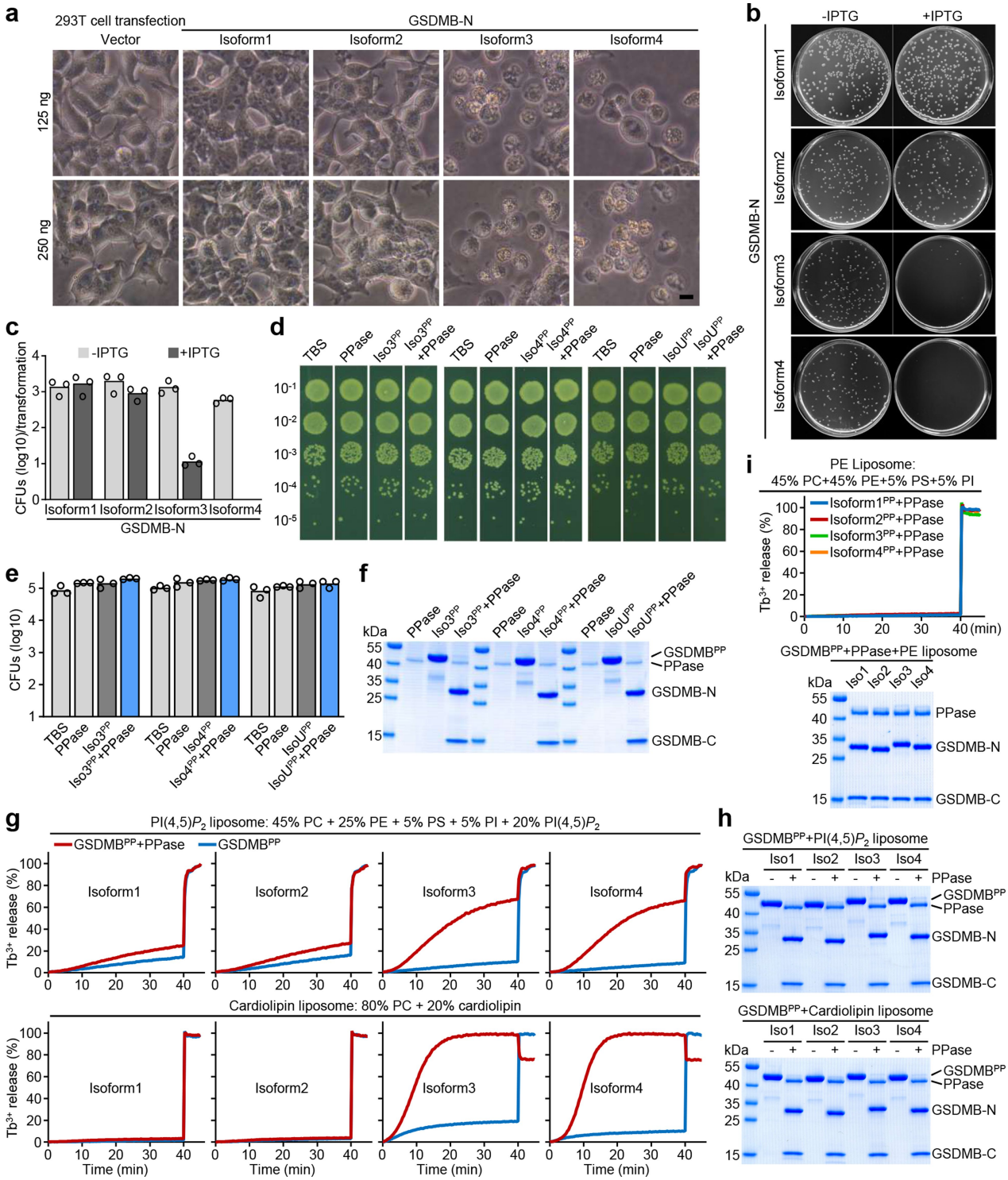

Extended Data Fig. 5 | Isoform-dependent pore-forming activity of GSDMB. **a**, Morphological assay of pyroptotic activities in different GSDMB isoforms. GSDMB-N domains derived from different isoforms were ectopically expressed in 293T cells. Scale bar, 25 μm. **b**, **c**, Cytotoxicity of GSDMB-N domains from different isoforms in bacteria. The N domains of indicated GSDMB isoforms under an IPTG-inducible promoter were transformed into *E. coli*. **b**, *E. coli* colonies on representative agar plates in the absence or presence of IPTG. **c**, Bacterial colony-forming units (CFU) per transformation of indicated isoforms are shown in the logarithmic form (log10), expressed as means (bars) of three replicates (circles). **d**–**f**, Direct CFU counting assay of the bacteriocidic activity in different GSDMB isoforms. The exponential-phase *S. flexneri* cultures were treated with the TBS media, purified PPase, or an indicated $GSDMB^{PP}$ isoform protein alone or being cleaved by the PPase. **d**, Serial dilution of the *S. flexneri* cultures on the agar plates. **e**, CFU counts of bacterial growth. **f**, SDS-PAGE analyses of PPase cleavage of the GSDMB isoform proteins. **g**–**i**, Liposome-leakage assays of pore-forming activity in GSDMB-N domains of different isoforms. Liposomes with indicated lipid compositions were treated with purified $GSDMB^{PP}$ in the presence or absence of PPase. **g**, Liposome leakage was monitored by measuring DPA chelating-induced fluorescence of the released Tb^{3+}. **h**, Cleavage of $GSDMB^{PP}$ by PPase was analyzed by SDS-PAGE. **i**, Assay of the pore-forming activity on the control PE liposomes. All data are representative of three independent experiments.

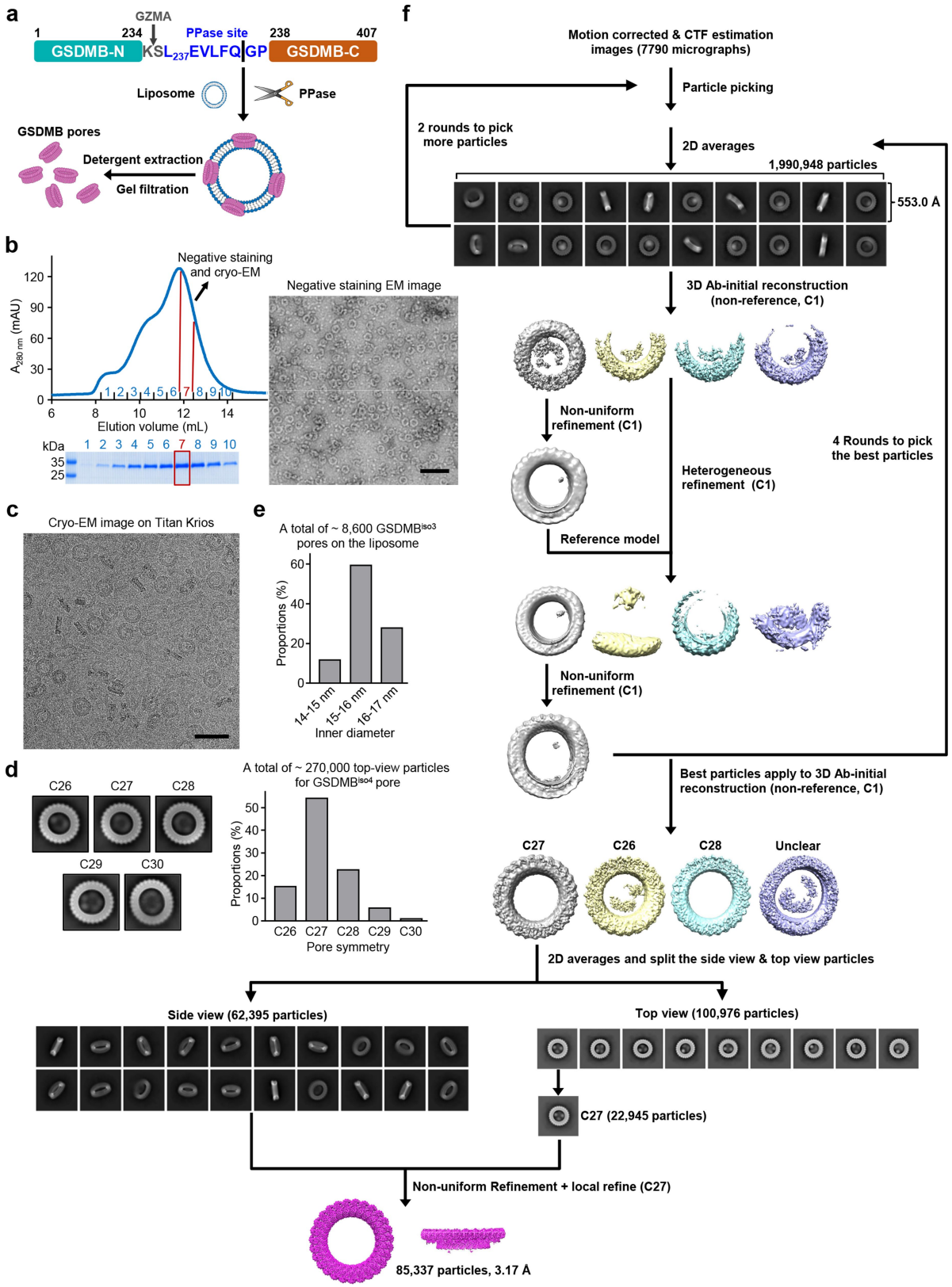

Extended Data Fig. 6 | See next page for caption.

Extended Data Fig. 6 | Preparation of GSDMB pore samples and cryo-EM data processing. a–**d**, Reconstitution, purification, and EM examination of GSDMB^{Iso4} pores. **a**, Schematic diagram illustrating reconstitution and extraction of GSDMB pores from the liposomes. **b**, Purification of GSDMB pores by gel-filtration chromatography. The highlighted fraction containing homogenous pores were analyzed by SDS-PAGE and also applied to negative-stain EM examination and final cryo-EM data collection. Negative-stain EM image of GSDMB pores (representative of three independent experiments) is shown. Scale bar, 100 nm. **c**, Cryo-EM micrograph of GSDMB pores (representative of 7790 micrographs). Scale bar, 50 nm. **d**, Percentages of GSDMB pores with C26, C27, C28, C29 and C30-fold symmetry among a total of 270,000 top-view pore particles. **e**, Pore size distribution for GSDMB^{Iso3}. Inner diameters of a total of 8,600 GSDMB^{Iso3} pores on the liposomes were measured. **f**, Processing of the cryo-EM dataset for GSDMB pore structure determination. Briefly, initial 3D model reconstruction generated a correct pore-like model. Iterative 2D and reference-guided 3D classifications were performed to select the best particles. A further round of 3D classification of the best particles indicates symmetry heterogeneity in the pores; a certain class of symmetry was chosen for final structural determination. Deep 2D classification allowed separation of the side view particles that were combined with best top view particles for 3D reconstruction and symmetry-imposed refinement to yield final cryo-EM maps.

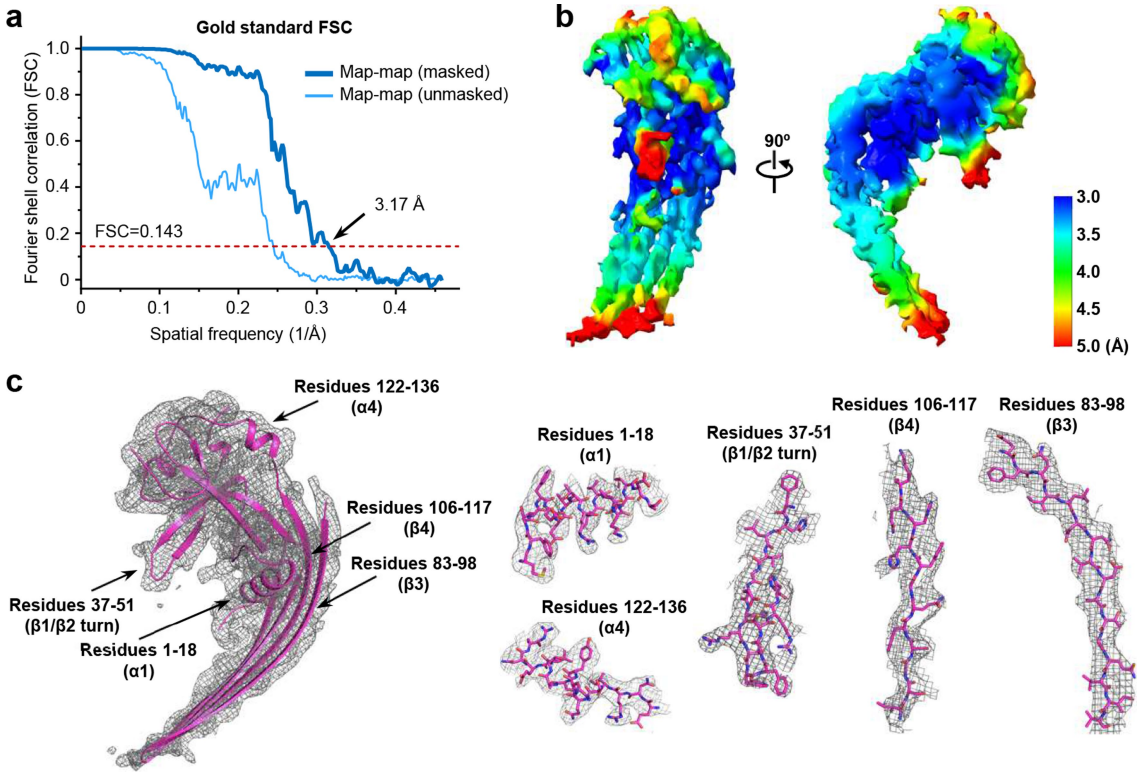

Extended Data Fig. 7 | Cryo-EM structural analysis of GSDMB pore. a, Gold-standard Fourier shell correlation (FSC) plot for the 27-fold symmetric GSDMB pore. Horizontal dashed lines represent FSC cut-offs at 0.143. **b**, The cryo-EM density map of GSDMB pore is colored based on local resolution estimated using RESMAP in CryoSPARC. **c**, Validation of the cryo-EM density map. Close-up views show GSDMB subunit model fitted into the density map at five indicated locations.

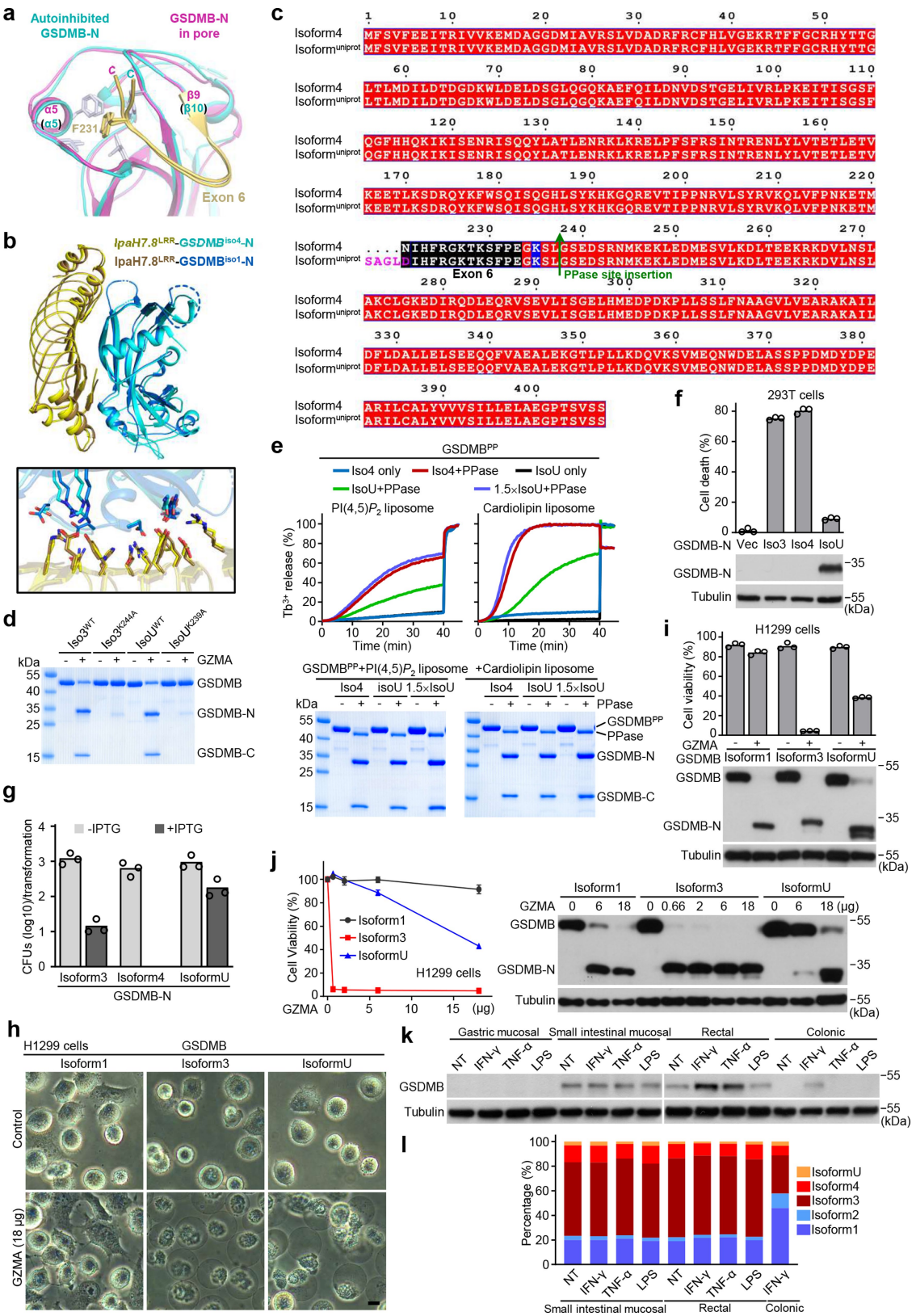

Extended Data Fig. 8 | See next page for caption.

Extended Data Fig. 8 | Structural and functional analyses of GSDMB isoforms and their relevance to cancer cell pyroptosis. a, Close-up view of structures around exon-6 region in the GSDMB-N domain. GSDMB-N structures in the autoinhibited state and in the pore are overlaid, with exon-6 regions highlighted in wheat. Relevant structural elements are labeled and crucial residues are in sticks. **b**, Superimposition of IpaH7.8^{LRR}–GSDMB^{iso1} and IpaH7.8^{LRR}–GSDMB^{iso4} complex structures. Close-up view shows the IpaH7.8–GSDMB binding interface in the two complexes and binding residues are in sticks. **c**, Sequence alignments of GSDMB^{IsoU} and GSDMB^{iso4}. Different residues are in magenta. Exon-6 sequences are in black background. GZMA cleavage site is in blue. Green arrow marks the site for inserting the PPase sequence. Identical residues are in red background. Numbers of starting residues are on top of the sequence. **d**, Cleavage of GSDMB^{IsoU} by GZMA. WT or the cleavage-site lysine mutant of GSDMB^{Iso3} or GSDMB^{IsoU} proteins were incubated with GZMA, followed by SDS-PAGE analyses. **e**, Assay of pore-forming activity in GSDMB^{IsoU}. Liposomes were treated with indicated isoforms of purified GSDMB^{PP} in the presence of PPase. Liposome leakage was monitored by measuring DPA chelating-induced fluorescence of released Tb^{3+}. SDS-PAGE analyses show cleavage of GSDMB^{PP}. **f**, **g**, Cytotoxicity of the GSDMB-N domain of indicated isoforms. **f**, Indicated GSDMB-N domains were transfected into 293T cells and their expression was probed by immunoblotting. LDH release-based cell death data are means (bars) of three replicates (circles). **g**, Indicated GSDMB-N domains under an IPTG-inducible promoter were transformed into *E. coli*. CFUs per transformation are shown in the logarithmic form (log10) as means (bars) of three replicates (circles). **h**–**j**, Analyses of the pyroptosis-inducing function of GSDMB^{IsoU}. H1299 cells stably expressing an indicated isoform were electroporated with a fixed dose (**h**, **i**) or titrating amounts of GZMA (**j**). **h**, Morphological examination of cell pyroptosis. Scale bar, 25 μm. **i**, **j**, Cleavage of GSDMB was probed by immunoblotting and ATP-based cell viability, expressed as means (bars) of three replicates (circles), is shown. **k**, **l**, Analyses of relative GSDMB isoform expression in primary epithelial cells derived from human gastrointestinal tissues. Indicated cells were left untreated (NT) or stimulated with IFN-γ, TNF-α, or LPS. **k**, GSDMB expression was examined by immunoblotting. **l**, Total mRNA transcripts of GSDMB were subjected to sequencing to quantify the different isoforms. Data are representative of three (**d**–**j**) or two (**k**, **l**) independent experiments. See Supplementary Fig. 1 for gel source data.

Extended Data Table 1 | X-ray data collection and refinement statistics

	$GSDMB^{iso1}$–$IpaH7.8^{LRR}$ (PDB 8GTK)	$GSDMB^{iso4}$–$IpaH7.8^{LRR}$ (PDB 8GTJ)
Data collection		
Space group	$P3_221$	$P3_121$
Cell dimensions		
a, b, c (Å)	102.73, 102.73, 121.32	88.34, 88.34, 335.62
α, β, γ (°)	90, 90, 120	90, 90, 120
Wavelength (Å)	1.00000	0.97852
Resolution (Å)	47.30-3.10 (3.31-3.10)	45.15-2.70 (2.77-2.70)
R_{merge} (%)	6.3 (104.6)	10.0 (87.5)
$I/\sigma I$	22.9 (2.7)	26.1 (3.3)
Completeness (%)	99.9 (99.3)	99.9 (100.0)
Redundancy	14.6 (15.2)	18.4 (19.6)
Refinement		
Resolution (Å)	47.30-3.10	45.15-2.70
No. reflections	13,637	42,916
R_{work}/R_{free} (%)*	26.81/28.96	24.23/27.60
No. atoms		
Protein	4,528	9,455
Water	-	152
B-factors (Å^2)		
Protein	135.72	63.37
Water	-	50.16
R.m.s deviations		
Bond lengths (Å)	0.010	0.005
Bond angles (°)	1.308	0.739
Ramachandran plot		
Favored (%)	97.44	95.71
Allowed (%)	2.56	4.29

Values in parentheses are for the highest-resolution shell. *, 5% of reflections are randomly selected for calculating R_{free}.

Extended Data Table 2 | Cryo-EM data collection, refinement and validation statistics

	GSDMB-pore (EMD-34258) (PDB 8GTN)
Data collection and processing	
Magnification	64,000
Voltage (kV)	300
Electron exposure (e^{-}/Å^2)	50
Defocus range (μm)	-1.0 ~ -2.0
Pixel size (Å)	1.08
Symmetry imposed	C27
Initial particle images (no.)	1,990,948
Final particle images (no.)	85,337
Map resolution (Å)	3.17
FSC threshold	0.143
Map resolution range (Å)	2.8 ~ 8.5
Refinement	
Initial model used (PDB code)	8GTJ
Model resolution (Å)	3.16/3.68
FSC threshold	0.143/0.5
Map sharpening *B* factor (Å^2)	-113
Model composition	
Non-hydrogen atoms	48,303
Protein residues	5,859
R.m.s. deviations	
Bond lengths (Å)	0.003
Bond angles (°)	0.539
Validation	
MolProbity score	1.82
Clashscore	15.34
Poor rotamers (%)	1.50
Ramachandran plot	
Favored (%)	99.06
Allowed (%)	0.94
Disallowed (%)	0

nature portfolio

Corresponding author(s): Feng Shao, Jingjin Ding

Last updated by author(s): Feb 9, 2023

Reporting Summary

Nature Portfolio wishes to improve the reproducibility of the work that we publish. This form provides structure for consistency and transparency in reporting. For further information on Nature Portfolio policies, see our Editorial Policies and the Editorial Policy Checklist.

Statistics

For all statistical analyses, confirm that the following items are present in the figure legend, table legend, main text, or Methods section.

n/a	Confirmed
☐	☒ The exact sample size (*n*) for each experimental group/condition, given as a discrete number and unit of measurement
☐	☒ A statement on whether measurements were taken from distinct samples or whether the same sample was measured repeatedly
☒	☐ The statistical test(s) used AND whether they are one- or two-sided *Only common tests should be described solely by name; describe more complex techniques in the Methods section.*
☒	☐ A description of all covariates tested
☒	☐ A description of any assumptions or corrections, such as tests of normality and adjustment for multiple comparisons
☐	☒ A full description of the statistical parameters including central tendency (e.g. means) or other basic estimates (e.g. regression coefficient) AND variation (e.g. standard deviation) or associated estimates of uncertainty (e.g. confidence intervals)
☒	☐ For null hypothesis testing, the test statistic (e.g. *F*, *t*, *r*) with confidence intervals, effect sizes, degrees of freedom and *P* value noted *Give P values as exact values whenever suitable.*
☒	☐ For Bayesian analysis, information on the choice of priors and Markov chain Monte Carlo settings
☒	☐ For hierarchical and complex designs, identification of the appropriate level for tests and full reporting of outcomes
☒	☐ Estimates of effect sizes (e.g. Cohen's *d*, Pearson's *r*), indicating how they were calculated

Our web collection on statistics for biologists contains articles on many of the points above.

Software and code

Policy information about availability of computer code

Data collection	XDS (version 20220110): Kabsch, 2010, https://xds.mr.mpg.de/
Data analysis	PHENIX (version 1.20.1): Liebschner et al., 2019, https://phenix-online.org/; Coot (version v0.9.8.1): Emsley et al., 2010, https://www2.mrc-lmb.cam.ac.uk/personal/pemsley/coot/; MolProbity (4.2): http://molprobity.manchester.ac.uk/; AlphaFold (version 2): https://alphafold.ebi.ac.uk/; PyMOL (version 2.5): The PYMOL Molecular Graphics System, Schrödinger, https://pymol.org/2/; ChimeraX (version 1.4): https://www.rbvi.ucsf.edu/chimerax/; MotionCorr2 (version 1.4.7): https://emcore.ucsf.edu/ucsf-software; CTFFIND (version 4): https://grigoriefflab.umassmed.edu/ctf_estimation_ctffind_ctftilt; CryoSPARC (version 3.3.1): https://cryosparc.com/; Blob-picker, Template-picker, and Heterogeneous Refinement programs are functional parts of CryoSPARC suite; Prism (version 8.3.0): GraphPad Software, https://www.graphpad.com/scientific-software/prism/;

For manuscripts utilizing custom algorithms or software that are central to the research but not yet described in published literature, software must be made available to editors and reviewers. We strongly encourage code deposition in a community repository (e.g. GitHub). See the Nature Portfolio guidelines for submitting code & software for further information.

Data

Policy information about availability of data

All manuscripts must include a data availability statement. This statement should provide the following information, where applicable:

- Accession codes, unique identifiers, or web links for publicly available datasets
- A description of any restrictions on data availability
- For clinical datasets or third party data, please ensure that the statement adheres to our policy

The atomic coordinates and structure factors generated in this study have been deposited in Protein Data Bank (PDB) under the accession codes 8GTJ, 8GTK and 8GTN. The following Protein Data Bank entries were used in this study: 6N9O, 5B5R, 6VFE and 6CB8). Source data are provided with this paper. All these structural data are available at https://www.rcsb.org/.

Human research participants

Policy information about studies involving human research participants and Sex and Gender in Research.

Reporting on sex and gender	Not applicable (no human research participants in this study).
Population characteristics	Not applicable (no human research participants in this study).
Recruitment	Not applicable (no human research participants in this study).
Ethics oversight	Not applicable (no human research participants in this study).

Note that full information on the approval of the study protocol must also be provided in the manuscript.

Field-specific reporting

Please select the one below that is the best fit for your research. If you are not sure, read the appropriate sections before making your selection.

☒ Life sciences ☐ Behavioural & social sciences ☐ Ecological, evolutionary & environmental sciences

For a reference copy of the document with all sections, see nature.com/documents/nr-reporting-summary-flat.pdf

Life sciences study design

All studies must disclose on these points even when the disclosure is negative.

Sample size	No sample size calculation was performed. This is mainly a structure and biochemistry study and does not involve any animal experiments. For sample size, we follow the general and routine practice for those standard biochemical and cellular experiments .
Data exclusions	There were no data exclusions.
Replication	All biochemical and cellular experiments have been repeated for at least three times to ensure reproducibility, which is the general practice in our lab. All attempts at replication in this study are successful. Experiments results were robust and reproducible. The difference between the experimental group and the control group was statistically significant in the repetitive experiments.
Randomization	No randomization was used in this study. This is mainly a structure study and other experiments are all standard cell culture and in vitro protein biochemical assays. Thus, it is well accepted and an established notion that randomization is not relevant to this kind of study.
Blinding	No blinding was done in this study. his is mainly a structure study and other experiments are all standard cell culture and in vitro protein biochemical assays. Thus, it is well accepted and an established notion that blinding is not relevant to this kind of study.

Reporting for specific materials, systems and methods

We require information from authors about some types of materials, experimental systems and methods used in many studies. Here, indicate whether each material, system or method listed is relevant to your study. If you are not sure if a list item applies to your research, read the appropriate section before selecting a response.

Materials & experimental systems

n/a	Involved in the study
☐	☒ Antibodies
☐	☒ Eukaryotic cell lines
☒	☐ Palaeontology and archaeology
☒	☐ Animals and other organisms
☒	☐ Clinical data
☒	☐ Dual use research of concern

Methods

n/a	Involved in the study
☒	☐ ChIP-seq
☒	☐ Flow cytometry
☒	☐ MRI-based neuroimaging

Antibodies

Antibodies used

Rabbit monoclonal antibodies against human GSDMB (ab215729/EPR20841), mouse GSDMD (ab219800/ EPR20859) were obtained from Abcam and anti-Myc antibody (HX1821) was obtained from Huaxing bio Inc. Antibodies against Flag (F3165/M2) and tubulin (T5168/ B-5-1-2) were purchased from Sigma-Aldrich. For western blot, horseradish peroxidase (HRP)-conjugated anti-mouse IgG (NA931/polyclonal) and HRP-conjugated anti-rabbit IgG (NA934/polyclonal) were purchased from GE Healthcare Life sciences. Antibodies for Flag, Tubulin were used at 1:5,000 dilution, and all other primary antibodies were used at 1:1,000 dilution. All the secondary antibodies for western blot were used at 1:5,000 dilution.

Validation

Antibodies for human GSDMB, mouse GSDMD, Myc, Flag and tubulin used to detect proteins in Western Blot, have been validated by the corresponding manufacturers and the detailed information can be found on the manufacturers' websites. Usage of all these primary antibodies has been well established in our laboratory after our own informal validation.

Eukaryotic cell lines

Policy information about cell lines and Sex and Gender in Research

Cell line source(s)

HEK293T, OVCAR-5, HT29, and COLO 205 cells were obtained from the American Type Culture Collection (ATCC). OE19, HCC1954, and OE33 cells were purchased from Cobioer Inc. H1299 cells (ATCC, CRL-5803) were a gift from Dr. X. Wang (National institute of Biological Sciences, Beijing, China). SW837 cells (ATCC, CCL-235) were kindly provided by Dr. X. Zhao (Air Force Medical University, China). NK-92MI cells (CRL-2408) were a gift from Dr. Z. Shen (BeiGene Inc.).

Authentication

Identity of the cell lines were frequently checked by their morphological features but have not been authenticated by the short tandem repeat (STR) profiling.

Mycoplasma contamination

All cell lines were tested to be mycoplasma-negative by the standard PCR method.

Commonly misidentified lines
(See ICLAC register)

No commonly misidentified cell lines are used in this study.